Isolating Single Cycles of Neural Oscillations in Spiking Activity

Ehsan Sabri[✉] **and Renata Batista-Brito**
Dominick P. Purpura Department of Neuroscience
Albert Einstein College of Medicine
1410 Pelham Parkway South, Bronx, NY 10461

Abstract

Neural oscillations are prominent features of brain activity, observable through frequency-specific power changes in electroencephalograms (EEG) and local field potentials (LFP). They also manifest as rhythmic coherence across brain regions. Although the identification of oscillations has primarily relied on EEG and LFP, the intrinsic relation between neural oscillations and neuronal ***spiking*** is noteworthy. We investigate the potential to detect individual cycles of neural rhythms solely through the spiking activity of neurons, leveraging recent advances in densely recording large populations of neurons within a local network. The numerous spikes from many neurons within a local network estimate the network's activity over time, enabling the identification of cyclic patterns. Here, we utilize a Long Short Term Memory (LSTM) network to effectively isolate and align individual cycles of neural oscillations from the spiking of a densely recorded population of neurons. This isolation occurs in the temporal domain, where cycles from different time scales may combine in various ways to shape the network's spiking probability. We simulated the population spiking probability by synthesizing a signal using the known neural cycles, such as gamma, beta, etc., as the basis functions. We also introduced noise and variations in the width of each cycle instance to match the spectral profile of the recorded population spikings. We then used this synthesized signal to train a multilayer LSTM network to detect the timing of the underlying cycles. We applied this network to robustly isolate specific cycles in different brain regions of mice across different time scales, from gamma to ultra-slow rhythms spanning durations of up to hundreds of seconds. These ultra-slow rhythms, which are usually cut off in the LFP, are also detected in behavioral measures of arousal, such as pupil size and mouse facial motion, and show delayed coherence with corresponding rhythms in the population spiking. We used isolated gamma cycles driven by sensory input to achieve a more precise alignment of the trials in sensory stimulation experiments in the primary visual cortex (V1) of mice. This alignment compensates for the biological variation in the transmission times of sensory signals from the retina to V1 across trials. As a result, we retrieve more accurate neural dynamics in response to sensory stimulation. Moreover, we applied this method to measure the correlated spiking across brain regions on different time scales. This involved isolating distinct cycles in population spiking of simultaneously recorded regions. We observed that the delay in population spiking between brain regions varies across different time scales.

[✉]Correspondence: `mohammad.sabri@einsteinmed.edu` github.com/esiabri/isoCycle

1 Introduction

Neural rhythms, which represent distinct cyclic temporal patterns of activity in the network, are fundamental features of neural systems (Buzsáki, 2006; Fries et al., 2001; Gray et al., 1989; Klimesch, 1999; Lakatos et al., 2008; Wang, 2010). These oscillatory patterns in neuronal population activity are primarily detected by measuring adjacent electromagnetic fields (Buzsáki et al., 2012). Rhythmic activity typically arises within particular spectral bands (Figure 1A) as observed in the Local Field Potential (LFP) (Buzsáki and Draguhn, 2004). Individual neurons tend to fire spikes during specific phases of these rhythms (Pesaran et al., 2002; Sirota et al., 2008). This suggests that the probability of neuronal spiking is modulated by the same recurring temporal motifs—namely, cycles (Figure 1B), which underlie the spectral changes observed in LFP. The duration of these cycles is linked to their respective frequency bands (Figure 1B). For example, a gamma cycle spans approximately 20 milliseconds. Spectral analysis of neural signals, especially of LFP, has been the primary method for establishing the correlation of rhythmic activities with various functions of the nervous system. Time-domain methods have also been developed to detect the cycles of repeating patterns in LFP (Cole and Voytek, 2019; Perrenoud et al., 2022). However, it is unclear to what extent the spiking activity of neurons contains information about the timing of individual cycles.

We hypothesize that the single occurrences of these cycles could be isolated if we reasonably estimate network activity over time from the recorded population spiking. In densely recorded extracellular activity, where tens of neurons are recorded simultaneously within a local network, we estimate fluctuations in network activity over time by examining changes in the recorded population spike count. Changes in the rate of collective network spiking reflect shared variations in the neuronal sub-threshold activity across the network. Sub-threshold activity has also been shown to follow LFP (Haider et al., 2016; Perrenoud et al., 2016). Taken together, these observations suggest that we can identify patterns of cyclic neural activity by analyzing network spiking.

To test this hypothesis, we employed Long Short Term Memory (LSTM) networks as decoders to isolate individual cycles of various neural rhythms. We accomplished this by analyzing the variations in the population spike rate in the time domain. LSTM is a powerful tool for analyzing time-series data, capable of considering the history of the signal to identify learned events (Hochreiter and Schmidhuber, 1997), which makes it well-suited for our investigation. We trained the decoder using a synthesized signal, constructed with neural cycles as basis functions (Figure 1B), and incorporated noise and variations in the width of each cycle instance to match the spectral characteristics of the biological signal (Figures S1 and 1B-C, Methods). Using the trained decoder, we then identified the timing of individual cycles underlying the fluctuations in the population spike counts during extracellular recording experiments.

Using this approach, we isolated individual cycles of distinct rhythms across multiple regions within the mouse brain. In the primary visual and somatosensory cortices (V1 and S1) of mice, we effectively isolated cycles with durations ranging from gamma (around 20 ms) to several hundred seconds. In visual stimulation experiments, we used isolated sensory-driven gamma cycles in V1 to improve trial alignment precision. This realignment compensated for variations in signal transmission times from the retina to V1 across trials. Furthermore, we applied this method to simultaneous recordings from tens of regions in the mouse brain (Steinmetz et al., 2019). We observed that the correlated activity patterns among these brain regions vary across time scales.

2 Results

2.1 Cycle Detection in Population Spiking of Mouse Primary Sensory Cortex

We developed a nonparametric, time-domain method to isolate individual cycles of neural oscillations from population spiking. For this cycle detection, we employed an LSTM network, functioning as a decoder (Figure 1C). This network was trained on synthesized signals constructed with known neural cycles, such as gamma, beta, and others, and we validated the decoder's performance with generated ground truth data (Figures S1 and 1B-C, Methods). To test the cycle detection in neuronal spiking, we recorded extracellular activity using single-shank linear silicon probes along the width of the primary visual cortex (V1, n=5) and the primary somatosensory cortex (S1, n=4) of head-fixed mice. In each recording session, we combined the spike times from all recorded neurons (n=55$\pm$31, mean$\pm$std across nine recording sessions) to identify the timing of individual cycles of the rhythms ranging

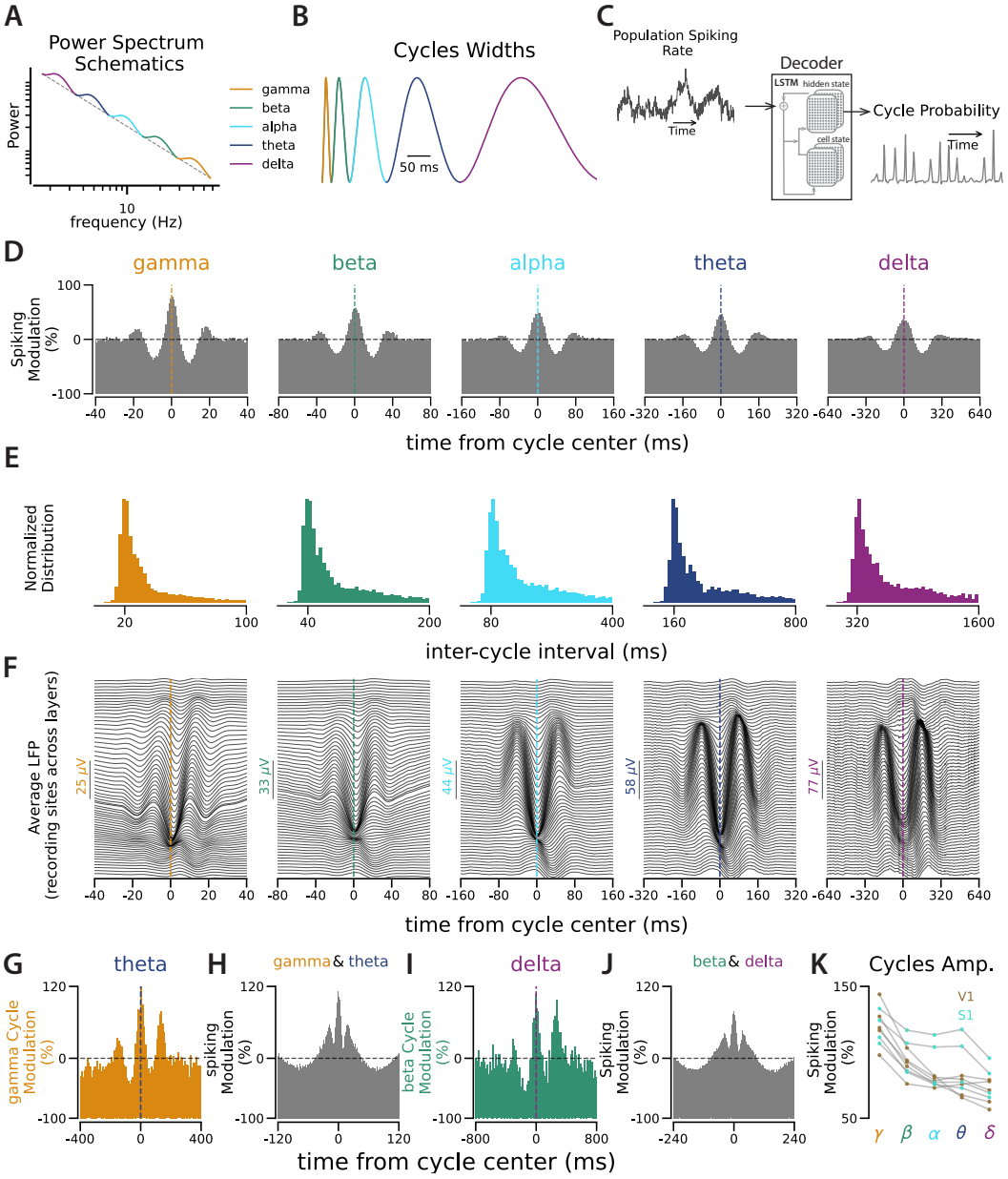

Figure 1. Cycle Detection in Population Spiking. A. Schematic illustrating the modulation of neural activity power spectrum across specific frequency bands commonly observed in neural recordings. The dashed line represents the 1/f power decrease in the spectrum, and the bumps represent the band-specific power modulations. Both axes are presented in logarithmic scale. **B.** Cycle width of rhythmic activities linked to spectral bands in A. **C.** The decoder evaluates the changes in network spiking over time and returns the probability of the targeted cycle type at each time point. The decision for cycle detection is made based on the decoder output (see Figure S1). **D.** Distribution of all population spike times aligned with detected cycle times for each cycle type during 6300 seconds of extra-cellular recording from 131 neurons in V1. 5000 cycle times were randomly chosen for each cycle type to generate this spiking distribution. The horizontal dashed line is the chance level (see Figures S2 and S3 for similar distributions around shifted and shuffled cycle times). The vertical line in each panel indicates the center of the detected cycles. The y-axis shows the amount of spiking modulation relative to the chance level. **E.** Normalized distribution of inter-cycle interval (ICI) for each cycle type, similar to panel D. **F.** Average LFP aligned with detected cycle times. Each panel corresponds to the cycle in the same column as in A. LFP was recorded with 64 channels across the width of the cortex. The upper traces correspond to channels in the superficial layers and the lower traces correspond to channels in deeper layers. Scales for each cycle type are adjusted for pattern visibility. **G.** Distribution of the gamma cycle times aligned with theta cycle times. **H.** Distribution of population spiking relative to co-occurrences of gamma and theta cycles. **I.** Distribution of the beta cycle times aligned with the delta cycle times. See Figure S4 for all pairwise relations of cycles. **J.** Distribution of population spiking relative to co-occurrences of beta and delta cycles. For spiking distributions relative to co-occurrences of other pairs of cycles, see Figure S5.

Figure 1. K. The Y-axis shows the trough-to-peak amplitude of the average shape of each cycle type, as in D, over 9 extracellular recordings: 5 recordings from V1 (brown) and 4 recordings from S1 (turquoise).

from gamma to delta (Figure 1C, Figure S1, Methods). We then used the times of the detected cycles for each cycle type to calculate the distribution of population spiking around each cycle type. These distributions represent the average cycle shape, as reflected in the spiking activity of the network (Figure 1D). To compare cycles across recordings and time scales, we normalized the average cycle shapes relative to the chance level, which is the average spiking during the recording (see Figures S2 and S3 for controls with shuffled and shifted detected cycle times). Normalized cycle shapes show how much the spiking modulation during each cycle type deviates from the baseline (i.e. chance level). Spiking modulation decreases across different time scales, moving from faster cycles like gamma to slower ones like delta (Figure 1K).

Do the detected cycles correspond to the known rhythmic patterns in the LFP? In the average cycle shapes, the recurring peaks, with positive and negative delays relative to the main peak (Figure 1D), indicate that it is likely to observe one cycle type right after the occurrence of the same cycle type, suggesting that these cycles of activity are recurring events. To characterize their rhythmicity, we examined the distribution of inter-cycle intervals (ICI), which measures the delays between consecutive cycles. These distributions show an isolated peak near the cycle width. For example, the peak of the ICI distribution for the gamma cycles is around 20 ms, consistent with the width of the gamma cycle (Figure 1E). To further examine the relation between the detected cycles in the spiking activity and the rhythmic patterns in the LFP, we calculated the average of LFP around the spiking-based detected cycles for each cycle type (Figure 1F). The average LFP around the detected cycles follows the cyclic patterns that we observed in the spiking activity. In faster cycles, such as gamma and beta, temporal delays in the spiking-based-detected LFP rhythms across the cortical layers suggest a propagation from deeper layers to more superficial layers (Saleem et al., 2017; Senzai et al., 2019).

How are various cycle types interrelated? For example, does the presence of a theta cycle influence the likelihood of observing a gamma cycle? It has been widely reported that neural rhythms across different bands are interrelated (Canolty et al., 2006; Canolty and Knight, 2010; Miller et al., 2018; Voytek et al., 2010): different rhythms are likely to happen simultaneously (amplitude coupling), and the faster rhythms tend to occur in certain phases of the slower rhythms (phase coupling). To investigate the cycle coupling, we examined the distribution of faster cycles given the presence of slower cycles (e.g., the distribution of gamma cycles conditioned on the observation of a theta cycle). We observed that faster cycles tend to occur at the peak of slower cycles, which provides the maximum efficiency in modulating spiking activity (Figure 1G-J, Figures S4 and S5).

2.2 Sensory-Driven gamma Cycles Capture the Variation in Signal Transfer Time between the Retina and V1 across Trials

To study neural dynamics in response to sensory stimulation, it is crucial to accurately align repeating sensory stimulation trials. During sensory stimulation experiments, we present the stimuli in several trials, and then, to compare the neural activity across trials, we align the trials based on the time of stimulus onset. However, this alignment method might not always be accurate, since the time taken for sensory information to reach the neural recording site can vary between trials. As gamma cycles have been shown to carry bottom-up sensory information (Bastos et al., 2020; Hoseini et al., 2021; Saleem et al., 2017), we used isolated sensory-driven gamma cycles to realign the trials.

After the alignment of trials based on the time of the first sensory-driven gamma cycles, we observed that the network response to sensory input goes through an increase followed by a decrease to baseline during 20-ms epochs. We estimate the network response to visual stimulation by examining changes in the number of recorded spikes, pooled from all the recorded neurons. Analyzing the network response across trials, relative to stimulus onset (Figure 2A&D), we observed that population spiking starts to increase and rises to a peak with a delay relative to stimulus onset (e.g., 50 ms is the peak time in the example recording session presented in Figure 2). The peak time in the trial-average response is the average signal transfer time between the stimulus onset and the arrival of the stimulus-related sensory information to the recording site. We used the time of the gamma cycle nearest to the average delay as the time of the first sensory-driven gamma cycle in each trial. After realigning the trials based

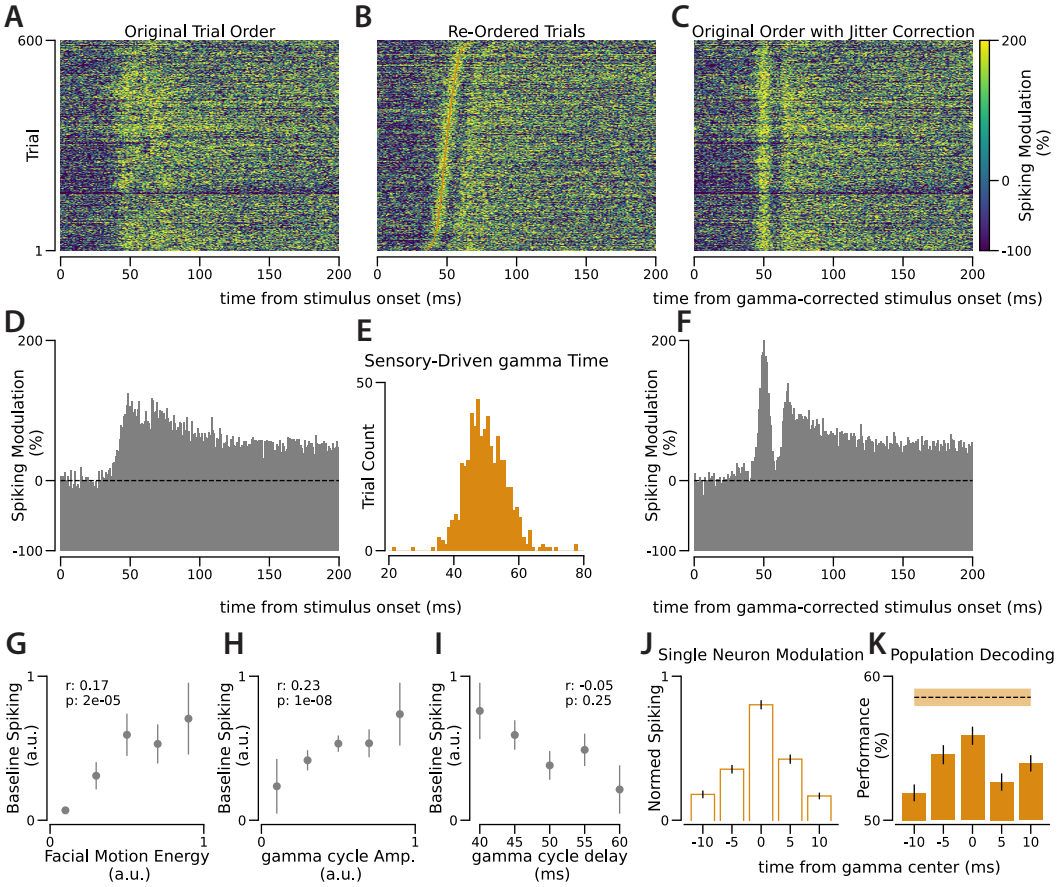

Figure 2. Using Sensory-Driven gamma Cycles to Capture the Biological Jitter across Trials. A. Spiking response to visual stimulation where each 1-ms time bin depicts the combined spiking modulation from 131 simultaneously recorded V1 neurons. Each row represents a trial of visual stimulation, with spiking values relative to the 200-ms pre-stimulus window average. **B.** As in A, the trials are reordered according to the timing of the first sensory-driven gamma cycle. Orange dots on each row indicate the center of these cycles. **C.** As in A, with the stimulus onset time adjusted based on varying sensory-driven gamma cycle timings across trials. **D.** Spiking average across trials, as shown in A. The y-axis shows the modulation of the population spiking relative to the baseline (represented by the dashed line). **E.** Distribution of the timing of the sensory-driven gamma cycle across trials, relative to stimulus onset. **F.** As in D, but after adjusting stimulus onset based on varying sensory-driven gamma cycle timings across trials. **G-I** Correlation of baseline spiking (from the 200-ms pre-stimulus window) across trials with **G.** facial motion, **H.** gamma cycle amplitude, and **I.** gamma cycle delay. Comparisons are made in 600 trials from the same recording session as other panels, and the correlation coefficients and the p-values result from Pearson correlation across these trials. The values of the baseline, facial motion, and gamma cycle amplitudes are normalized between 0 and 1. The trials are segmented into five groups within each panel; dots and lines represent the mean and s.e.m., respectively. **J.** Comparison of average spiking across 131 individual neurons for 5-ms bins during the first sensory-driven gamma cycle. The spiking of each neuron is normalized between 0 and 1 individually across the five time bins. **K.** Population decoding performance in determining stimulus orientation (horizontal vs. vertical) across 5-ms bins during the first sensory-driven gamma cycle. The dashed line illustrates performance when spikes from the entire gamma cycle are combined. The shaded area and the lines represent s.e.m. For similar analysis from additional sessions, refer to Figures S7 and S8.

on the timing of the first sensory-driven gamma cycle, we observe that the network spiking undergoes a cyclic pattern, an increase followed by a return to baseline, in response to sensory stimulation (Figure 2B, C, and F). The width of this cycle is close to the gamma, suggesting that the visual cortex receives sensory information in gamma-width packets.

To determine whether an individual sensory-driven gamma cycle carries sensory information, we employed population decoding in 5-ms bins during the first sensory-driven gamma cycle. In the recording sessions with drifting gratings as visual stimuli, we decoded horizontal versus vertical stimuli based on the activity of neurons in different phases of the gamma cycle. We found that the 5-ms central bin of the gamma cycle contains the most information about orientation, while the decoding capacity diminishes in both the preceding and subsequent phases of this 20-ms gamma cycle (Figure 2K).

2.3 Correlated Activity across Brain Regions in Different Time Scales

Coherent neural activity, characterized by synchronized rhythmic patterns, is considered a measure of information transfer between brain regions (Fries, 2015). This coherence, measured primarily using LFPs recorded in different brain regions, has been observed across various time scales and species (Brincat et al., 2021; Schneider et al., 2021; Schoffelen et al., 2005). This coherence has been attributed to various cognitive functions (Bastos et al., 2015; Buschman and Miller, 2007; Michalareas et al., 2016). We aimed to study the intra-areal coherence in the spiking activity across different time

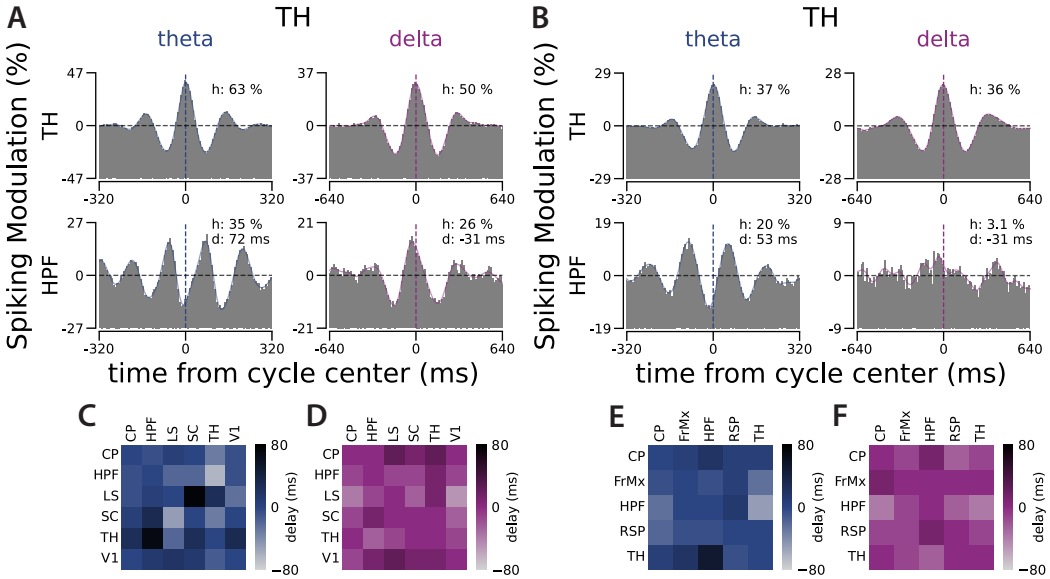

Figure 3. Correlated Dynamics Between Brain Regions Varies across Different Time Scales. A. The cycles detected in a recording site in the Anteromedial (AM) nucleus of the Thalamus (TH) were used to generate the distribution of spiking activity of two recording sites relative to theta and delta cycles in the TH: the first row is the distribution of spiking within the same Thalamical recording site relative to theta and delta cycles in the TH, the second row is the distribution of spiking in a recording site in the CA3 region of the Hippocampus (HPF) relative to the cycles in the TH. In each distribution, *h* represents trough-to-peak modulation relative to the chance level (the horizontal dashed line) and *d* represents the distribution peak delay relative to the center of the cycle in the reference region. **B.** Similar to A, but in a recording of a different animal, where cycles were detected at another AM Thalamic site. The distribution of spiking activities relative to these cycles is from the TH itself in the first row and the CA1 region of HPF in the second row. See Figure S9 for the results of the half-session control analysis for panels A and B. See Figures S10 to S12 for the distribution of the spiking activity of all the recorded regions relative to the cycles detected at these recording sites in TH in these two animals and relative to a recording site in HPF in another animal. For figures representing the pairwise relations across all recorded regions of the 3 animals in Steinmetz et al. (2019) see Sabri (2023). **C.** Pairwise delays between regions during theta cycles in the same recording as in A. **D.** Same as C for delays during the delta cycles. **E-F.** Same as C and D, for the same recording as in B. See Figure S13 for pairwise delays across all recorded regions for gamma to delta cycles in 3 animals.

scales. To achieve this, we applied cycle isolation to a dataset that had simultaneous recordings from multiple brain regions (Steinmetz et al., 2019). In each region's population spiking, we identified cycles across different time scales. Then, we computed the average spiking patterns in other regions relative to the detected cycles in the reference region, considering each cycle type separately.

Using the isolated cycles in the population spiking of a reference region, we constructed the distribution of spiking in other regions relative to each cycle type in the reference region. The generated distributions represent patterns of correlated spiking between pairs of regions, separately in each time scale. These intra-areal spiking correlation patterns reveal consistent, time scale-dependent delays between the spiking of different regions. For example, as shown in Figure 3A, during the theta cycle, the spiking of the Anteromedial nucleus of the Thalamus (TH) is half a cycle out of phase relative to the spiking in the CA3 region of the Hippocampus (HPF). However, for the slower delta cycle, the spiking in these two regions is lagged by one-tenth of a cycle duration. For faster cycles like gamma and beta, coherent activity (albeit delayed) is evident only between recording sites in highly connected areas, such as visual areas in the cortex or different regions of the HPF. As we examine the slower cycles, we observe that an increasing number of regions exhibit coherence (Figure S13, Sabri (2023)).

2.4 Isolating Ultra Slow Cycles in Population Spiking, Pupil Size, and Facial Motion

By isolating cycles in neuronal spiking, we can also study slower rhythmic activities typically filtered out in the LFP. Ultra-slow oscillations (< 1 Hz) have been shown to be a significant feature of neural activity across brain regions and species and correlate with cognitive functions and distinct network activity modes (Cogno et al., 2022; Cowley et al., 2020; Higley and Cardin, 2022; Leopold et al., 2003; Nunez-Elizalde et al., 2022; Okun et al., 2019; Vanhatalo et al., 2004).

What are the cycle widths of the ultra-slow rhythms (Table 1)? It has long been noted that the bandwidth of neural rhythms is nearly doubled from one band to the next. Numbers between the Golden Ratio, 1.618 (Pletzer et al., 2010; Roopun et al., 2008), and the Euler number, 2.7182 (Buzsáki and Draguhn, 2004; Penttonen and Buzsáki, 2003) have been suggested for this ratio between consecutive bands. However, the value two for the ratio matches the experimental observations better and ensures the maximal efficacy of coupling across bands (Klimesch, 2013). As one moves from one band to the next slower one, the spectral bandwidth decreases by half, and the cycle duration of these rhythms doubles (e.g., around 20 ms for gamma cycles, 40 ms for beta cycles, and so on, Figure 1A-B). Starting from a 20-ms cycle duration for gamma and doubling it, we arrive at a rhythm with a cycle duration of around 2.6 seconds, which is called "slow 2" by Buzsáki and Draguhn (2004). To name a broader range of slow rhythms, we termed it the e cycle (with reference to the Euler number) and named the other non-named slow cycles with reference to this one as $quarter\ e$, $half\ e$, $2e$, $4e$, $8e$, $16e$, and so on (Table 1).

Table 1. Approximate Cycle Durations

Cycle Name	Duration		Cycle Name	Duration		Cycle Name	Duration	
$gamma$	20	ms	$quarter\ e$	640	ms	$8e$	20	s
$beta$	40	ms	$half\ e$	1.25	s	$16e$	40	s
$alpha$	80	ms	e	2.5	s	$32e$	80	s
$theta$	160	ms	$2e$	5	s	$64e$	160	s
$delta$	320	ms	$4e$	10	s	$128e$	320	s

The cycle detection method that we introduced for population spiking can also be applied to changes in pupil size and the facial movements of mice. Here, we present the results of the cycle isolation of the ultra-slow rhythms in population spiking of the recorded neurons in mouse V1 and S1. We also show results from searching for similar cycles in pupil size changes and facial motion (Figures 4 and S14 to S17). These were recorded simultaneously with extracellular activity. The average activity around the detected cycles in each distinct ultra-slow time scale indicates a significant modulation in spiking activity, pupil size, and facial motion, although these modulations are less pronounced than in the faster cycles. The coherence across the modalities (spiking vs. pupil size vs. facial motion) during each cycle type indicates specific correlated dynamics. In particular, during ultra-slow cycles

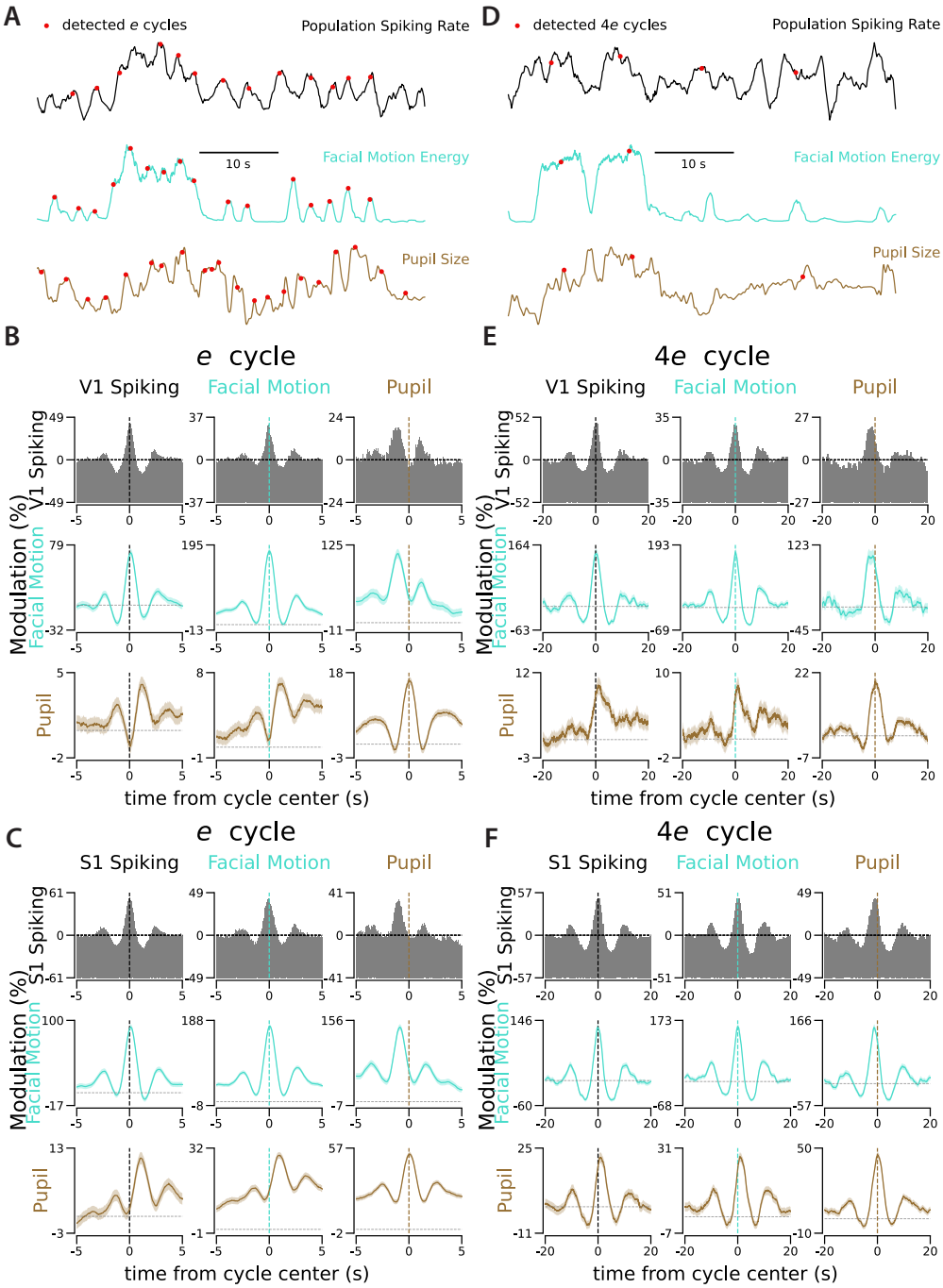

Figure 4. Ultra-Slow Cycles in Pupil Size and Facial Motion Appear with Delays Relative to Similar Cycles in V1 and S1. A. Example traces of population spiking rate, facial motion, and pupil size changes in the sample recording from V1. The red dots indicate the centers of the e cycles detected individually on each trace. All traces are normalized between 0 and 1 in this example window. **B.** Each panel shows the correlated activity between the target modality (e.g., facial motion signal on the second row) and the times of detected e cycles in the reference modality (e.g., V1 spiking in the first column). **C.** Same as B for a sample recording from S1. **D.** Same as A with red dots indicating the center of the detected $4e$ cycles. **E-F**. Same as B-C for $4e$ cycles. See Figures S14 to S17 for similar correlated activity during other slow cycles (Table 1) in these two recordings from V1 and S1. The vertical lines show the center of the detected cycles in the reference modality. The horizontal line in each panel shows the chance level. The vertical axes depict the modulation in the target modality relative to the chance level. The shaded area is s.e.m..

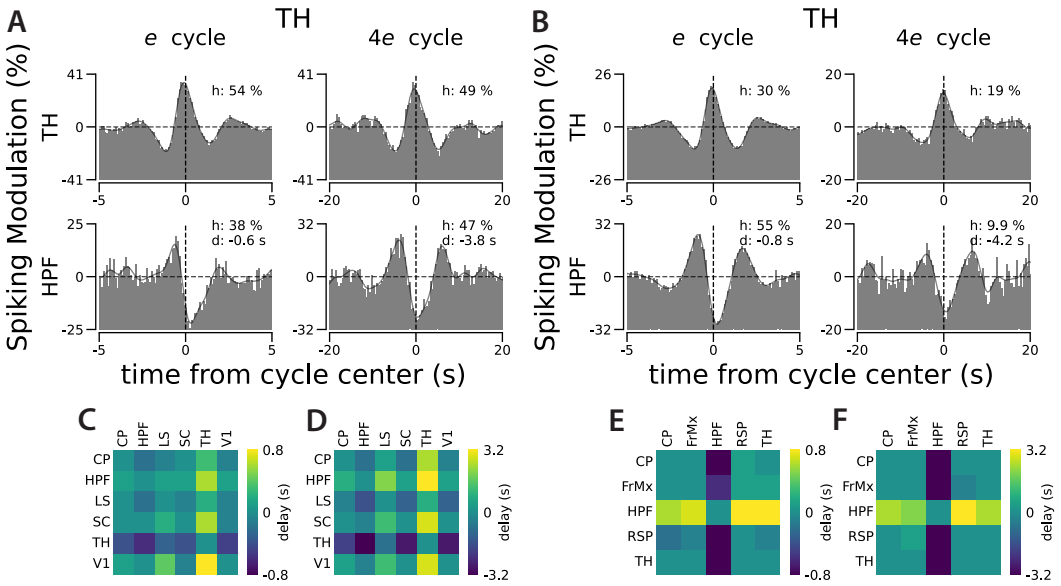

Figure 5. Ultra-Slow Cycles are Also Delayed Across Regions. A. Cycles detected in a recording site in the Thalamus (TH) were used to generate the spiking distribution in two recording sites relative to the e and $4e$ cycles in the TH: The first row is the distribution of spiking within the same Thalamic recording site relative to the e and $4e$ cycles in the TH, the second row is the distribution of spiking in a recording site in Hippocampus (HPF) relative to the cycles in the TH. In each distribution, h represents trough-to-peak modulation relative to the chance level (the horizontal dashed line) and d represents the distribution peak delay relative to the center of the cycle in the reference region. **B.** Similar to A, but in a recording of a different animal, cycles were detected at another Thalamic site. As in A, the first row depicts spiking from TH and the second from HPF. See Figures S18 to S20 for the distribution of spiking activity across all recorded regions relative to the $quarter\ e$ to $4e$ cycles detected within the TH sites of these two animals and an HPF site from another. For figures representing the pairwise relations across all recorded regions from the 3 animals in Steinmetz et al. (2019) in all cycles up to $128e$, see Sabri (2023). **C.** Pairwise delays across regions during e cycles, as observed in A's recording. **D.** Same as C for delays during $4e$ cycles. **E-F.** Same as C and D, as observed in B's recording. See Figures S21 and S22 for the pairwise delays across all recorded regions for the $quarter\ e$ to $64e$ cycles in 3 animals.

in both V1 and S1, the population spiking is in synchronized coherence with facial motion but is followed by the pupil with a delay of up to 1 second (Sabri and Batista-Brito, 2023).

The ultra-slow cycles detected in spiking across the mouse brain reveal a specific order of activation of regions during multi-second cycles. We isolated the ultra-slow cycles (Table 1) individually in each brain area during spontaneous activity recordings with eight neuropixel probes (Steinmetz et al., 2019). We observed specific temporal dynamics of correlated activity across brain regions, which depend on the time scales. For instance, as shown in Figure 5, the two recording sites in TH and HPF are 600 ms delayed during the e cycles, but 3.8 s delayed during the $4e$ cycles. We summarize the delays between all pairs of recorded regions in this dataset in delay matrices for each cycle type (Figures S21 and S22). For additional profiles of correlated activity, refer to Figures S18 to S20. Profiles of correlated activity across all pairs of recorded regions, spanning all time scales (from gamma to $64e$) and across 3 animals, can be found in Sabri (2023).

3 Discussion

We introduced a method for isolating single cycles of rhythmic patterns in the spiking of densely recorded populations of neurons. We applied this cycle isolation method to densely recorded neurons across the width of the cortex in mice V1 and S1 using single-shank probes. We found that the cycles captured in the population spiking reflect similar rhythmic patterns observed in the LFP. One advantage of cycle detection in spiking activity, instead of LFP, is that the spatial distribution of contributing neurons can be specified; for example, it is possible to detect the cycles separately in superficial and deep cortical layers using the neurons in each layer, while the measured LFP

in each layer is affected by the activity in other layers and cannot be used for independent cycle detection across layers. The isolated cycles also demonstrate the cross-frequency couplings by showing specific patterns of co-occurrence probability for pairs of different cycle types. In sensory stimulation experiments in V1, we used detected sensory-driven gamma cycles to realign the trials. This trial realignment compensates for the biological variation in the travel time of sensory signals between the retina and V1 and suggests that sensory information is conveyed in discrete temporal packets of activity. This idea is closely related to the proposal of temporal-packet-based activity (Luczak et al., 2013, 2015), generalized across different time scales. We further applied this method to isolate multi-second cycles in population spiking, facial movements, and pupil size changes. Using another dataset (Steinmetz et al., 2019), we also observed time-scale-dependent dynamics in correlated spiking across mouse brain regions. The brain-wide ultra-slow cycles, also reflected in pupil size and facial motion, may represent the physiological mechanisms driving behavioral states that are employed by neuromodulators such as Acetylcholine (Goris et al., 2014; Harris and Thiele, 2011; Lohani et al., 2022; Sabri and Batista-Brito, 2023; Sabri and Arabzadeh, 2018).

Are neural rhythms essential features of neural systems that play a necessary role in information processing and transfer (Singer, 1999)? Or are they just epiphenomena of these processes, lacking a functional role (Shadlen and Movshon, 1999)? Or do they fall somewhere in between? Neural rhythms and their correlation with brain function have primarily been identified through LFP and EEG measurements. However, spectral analyses and auto/cross correlograms of single neuron spiking have also revealed neural rhythms, particularly in networks with strong and persistent rhythmicity such as the theta rhythms of the rodent hippocampus (Buzsáki et al., 1983) and the rhythms in the cat visual cortex (Engel et al., 1991). Furthermore, with recent advancements in capturing single-trial dynamics in population activity (Pandarinath et al., 2018; Williams et al., 2020), neural rhythms were detected in single-cell spiking by correcting the across-trials jitters during cognitive tasks (Odean et al., 2023). However, the debate about the possible causal role of neural rhythms in brain function continues (Singer, 2018).

To shed light on this controversy, an answer to a related question will be helpful: How much of the rhythmicity observed in the LFP can be captured solely from spiking activity? The LFP measures population activity. It reflects rhythmicity when nearby axons transfer synchronized rhythmic input to the network or when nearby neurons share synchronized subthreshold rhythms. If the input axons or the nearby neurons carry rhythmic signals that are not synchronized, they are canceled out in the effective extracellular fields we measure. Thus, when searching for rhythmicity, the spiking activity of individual neurons is underpowered compared to the LFP. As a population measure of the spiking activity, the spikes from the nearby cells can be combined (Okun et al., 2019) to examine the fluctuations in the population spike count over time. This population firing rate reflects the shared variation in the membrane potentials of nearby neurons. Thus, it can serve as a spiking-based population measure, containing information about network cyclic activities comparable to the LFP.

Isolating individual cycles of neural rhythms in the time domain offers a deeper perspective on the dynamics of neural activity. Spectral analysis, the primary tool for detecting rhythmicity, is particularly effective when strong similar cycles occur multiple times right after each other. Spectral analysis successfully captures neural rhythms, especially when strong rhythms are locked to an external event and the noise has been reduced by averaging across trials. However, in single-trial spike trains, if similar cycles that modulate the probability of network spiking are irregular and of variable duration, the power spectrum may not capture the cycles as the underlying basis functions (Figure S1A). Thus, a robust time-domain method that detects single cycles in such conditions is desirable. Time domain methods developed to capture individual events in LFP and EEG (Cole and Voytek, 2019; Perrenoud et al., 2022) have been used to characterize neural cyclic events, such as their rate, shape, and contribution to the power spectrum (Cole and Voytek, 2017; Donoghue et al., 2020; Voytek et al., 2015).

We utilized an LSTM network, a powerful machine learning tool to incorporate the history of signal for event detection, in the time-domain to estimate the likelihood of a specific cycle type at each moment within a spike train. The main assumptions that have been introduced to our decoder during training are that 1) cycles have a Gaussian shape, and 2) there is a doubling relation between consecutive cycles. These assumptions are biologically plausible and match the experimental observations (Klimesch, 2013). To further validate these assumptions, we next need to employ an unsupervised method to identify the optimal basis functions that can best reconstruct local population spiking and/or LFP. Once these basis functions are identified, we can then develop customized decoders for

cycle detection, which might vary across species and brain regions. If these cyclic patterns of activity are proven to be the basis functions of the neural signal, it would suggest a biophysical constraint on the neural activity patterns: a population of neurons can just be activated by temporal patterns that are a linear summation of a specific set of cycles.

In this work, we demonstrated the ability to extract and align cycles of neural activity directly from neuronal spiking in a local population. For cycle isolation, we used a time-domain approach with an LSTM network trained on synthesized data. We applied these isolated cycles to: 1) compensate for jitter in signal transmission time from the retina to V1, 2) demonstrate the time-scale dependency of correlated activity dynamics across mouse brain regions, and 3) reveal the cyclic correlation between neural activity and behavioral measures of arousal in slow time scales.

4 Methods

4.1 Animals, Headpost Surgery, and Treadmill Habituation

All animal handling procedures were performed in accordance with guidelines approved by the Albert Einstein College of Medicine Institutional Animal Care and Use Committee and federal guide. We handled wild-type male mice, aged 3 to 5 months, for 10 to 15 minutes daily for three days prior to headpost surgery. On the day of surgery, the mouse was anesthetized with isoflurane and the scalp was cleaned with Betadine solution. After making a midline incision, the scalp was resected to expose the skull. A tungsten wire (50 μm) was then inserted into the right cerebellum through a small hole. This tungsten wire was connected to a gold-plated pin (World Precision Instruments) to serve as the ground/reference connection during electrophysiology recording. The reference pin and a custom 3D printed headpost were affixed to the skull using dental cement. However, the target recording site (either V1 or S1 in the left hemisphere) was left free from cement and was merely sealed with vetbond. After surgery, analgesics were administered to help with recovery. Following a 3- to 5-day recovery period after surgery, the mice began treadmill training. Over the next four days, we gradually increased the time the mice were head-fixed on the treadmill, continuing until they appeared comfortable and started running without obvious stress.

4.2 Electrophysiology, Behavioral State Monitoring and Visual Stimulation

Approximately 16-20 hours before the recording, a small craniotomy was performed over the designated recording site under light anesthesia using isoflurane, ensuring the dura remained intact. After craniotomy, the site was sealed with Kwik-Cast (World Precision Instruments), and the animal was allowed to recover in preparation for the recording session the next day. Single-shank 64-channel silicon probes (Sharpened H3, Cambridge NeuroTech) were used for the recordings. The probe was inserted 1200 μm deep from the dura at a rate of 1 μm/s and then retracted by 100 μm for faster stabilization. The broadband signal was recorded using an RHD USB interface board (Intan) at a rate of 20 kSample/s. For the LFP, the broadband signal from each channel was low-pass filtered (< 200 Hz) and downsampled to 2 kSample/s. To reduce shared high-frequency noise, the signal from each channel was high-pass filtered (> 300 Hz) and subtracted by the median of the high-pass filtered signals across the 64 channels at each time point. These median-corrected high-pass filtered signals were then processed to extract spike times using KiloSort (Pachitariu et al., 2016). The KiloSort output was manually curated to discard non-spike patterns.

The left half of the mouse face was recorded with the BFLY-PGE-13S2M-CS camera (FLIR) at 30 frames/s under infrared illumination. The recorded frames were synchronized with the electrophysiology signal using the TTL pulses the camera sends out during each frame's lens opening. The facemap software was used to extract the pupil size and facial motion (Syeda et al., 2022). To track facial movement, a rectangular window containing the whiskers and nose was selected.

For visual stimulation, a 1080x1920p gamma-corrected portrait mode Asus ROG PG248Q monitor was placed 20 cm from the right eye of the animal. This monitor was derived at 180 Hz (inter-frame-interval < 6 ms) with a GTX 1080Ti graphic card with g-sync disabled. Custom Matlab code with Psychtoolbox (Brainard, 1997) was used for stimulus presentation. The stimulus onset was detected using an SM1PD1A photodiode (Thorlabs). The rise time of the stimulus onset was measured with the photodiode signal being less than 2 ms. For visual stimulation, drifting gratings or natural images were presented to the animal. In the drifting grating sessions, 12 directions (30° apart starting from 0)

were used. The drifting gratings consisted of equal-sized (5 cm wide) full-contrast white and black bars with a temporal frequency of 2 Hz. Each direction was presented for 2 seconds in 50 trials with a variable 1.5-2 seconds gray screen intertrial interval. The order of 600 trials was randomized. In sessions with natural stimuli, 70 stimuli from ImageNet (Deng et al., 2010) were presented to the animal. Each stimulus was presented for 1 second in 27 trials with a variable 0.75-1 second gray screen inter-trial interval. The order of 1890 trials was randomized.

To evaluate neural activity in response to visual stimulation, the change in spiking after stimulus onset was quantified relative to baseline spiking. The baseline was defined as the average spiking in the 200 ms window prior to stimulus onset. To estimate the network response (Figure 2A-I), spikes from all neurons recorded in each session were pooled together. For the population decoding of the orientations presented in 5-ms bins (Figure 2K), the 12 directions were reduced to 2 orientations (horizontal vs. vertical) by combining nearby orientations. This reduction was necessary because the number of spikes from each neuron in 5-ms bins is very sparse to distinguish between many conditions when the number of recorded neurons (55 neurons on average in our dataset) is limited. A Support Vector Machine (SVM) was then used to decode the presented orientation from the neuronal spiking (Pedregosa et al., 2011). The training-to-testing trial ratio was set at 4:1 and the train/test was repeated 100 times, randomly selecting trials in each iteration.

4.3 Cycle Detection

For the cycle isolation, a network of Long Short Term Memory (LSTM) units was trained on synthetic data using the TensorFlow package (Abadi et al., 2015; Glaser et al., 2020). The LSTM network consisted of two layers of 200 units each. The input is sampled at 30 samples/cycle, differently for each target cycle. The input to the network at each time point consists of 61 samples, including 30 samples before and 30 samples after the current time point. The output layer of the network consists of one dense unit with linear activation. To introduce noise to the signal during training, a Gaussina_Noise layer (stddev: 0.05) was added immediately after the input layer. A synthesized signal with 3 million samples was used to train the network. The synthesized signal was generated using seven cycle types as basis functions. The duration of each cycle type doubled relative to the previous one (3 cycles shorter and three cycles longer than the target cycle for detection). Each type of cycle occurred with a 60% chance. Different cycle types are randomly combined in all possible ways, while cycles of the same type do not overlap. The width of each cycle at each instance was randomly jittered by adding a value derived from a normal distribution with $\mu = 0$ and σ set to 30% of the cycle width. These parameters were chosen so that the spectral density of the synthesized signal matches the average spectral density of the population firing rate at 29 recording sites across the mice brain from two datasets (Figure S1A). During training, the network output was set as a binary one-dimensional time series of the same length as the input. This output signal was set to zero everywhere except at the center of the target cycle. After training, network performance was evaluated using a ground-truth signal. An optimal threshold was chosen, based on the receiver operating characteristic (ROC) curve of the decoder, to decide the detected cycle times of the network output (Figure S1B-D). The trained network, along with the functions to apply it to neuronal spiking, is accessible at github.com/esiabri/isoCycle.

To quantify the average shape of each cycle (defined as the population spiking distribution relative to detected cycle times and normalized by chance level), we measured the height change from the left trough to the peak of the distribution (Figure 1D). Similarly, to quantify the coherence between two regions (defined as the population spiking distribution in the target region relative to the detected cycle times in the reference region and normalized to the chance level), we measured the trough-to-peak height and the delay of the peak of the distribution (see the bottom rows in Figure 3A-B for example coherence patterns between recording sites in TH and HPF). The coherence patterns, as well as the quantified coherence strength and delay for all region pairs and cycles (from gamma to $64e$) of the three animals in Steinmetz et al. (2019), are available in Sabri (2023). The quantification of the coherence pattern was performed only if it exceeded a p-value threshold of <0.01 in the Kolmogorov-Smirnov test compared to a uniform distribution. In each coherence pattern, the insets provide details on the exact p-value (p), coherence strength (h), and delay (d) (for examples, see Figures S10 to S12 and S18 to S20).

References

Abadi, M., Agarwal, A., Barham, P., Brevdo, E., Chen, Z., Citro, C., Corrado, G. S., Davis, A., Dean, J., Devin, M., Ghemawat, S., Goodfellow, I., Harp, A., Irving, G., Isard, M., Jia, Y., Jozefowicz, R., Kaiser, L., Kudlur, M., Levenberg, J., Mané, D., Monga, R., Moore, S., Murray, D., Olah, C., Schuster, M., Shlens, J., Steiner, B., Sutskever, I., Talwar, K., Tucker, P., Vanhoucke, V., Vasudevan, V., Viégas, F., Vinyals, O., Warden, P., Wattenberg, M., Wicke, M., Yu, Y., Zheng, X., and Research, G. (2015). TensorFlow: Large-Scale Machine Learning on Heterogeneous Distributed Systems.

Bastos, A. M., Lundqvist, M., Waite, A. S., Kopell, N., and Miller, E. K. (2020). Layer and rhythm specificity for predictive routing. *Proceedings of the National Academy of Sciences of the United States of America*, 117(49):31459–31469.

Bastos, A. M., Vezoli, J., Bosman, C. A., Schoffelen, J. M., Oostenveld, R., Dowdall, J. R., DeWeerd, P., Kennedy, H., and Fries, P. (2015). Visual areas exert feedforward and feedback influences through distinct frequency channels. *Neuron*, 85(2):390–401.

Brainard, D. H. (1997). The Psychophysics Toolbox. *Spatial vision*, 10(4):433–436.

Brincat, S. L., Donoghue, J. A., Mahnke, M. K., Kornblith, S., Lundqvist, M., and Miller, E. K. (2021). Interhemispheric transfer of working memories. *Neuron*, 109(6):1055–1066.

Buschman, T. J. and Miller, E. K. (2007). Top-down versus bottom-up control of attention in the prefrontal and posterior parietal cortices. *Science (New York, N.Y.)*, 315(5820):1860–1864.

Buzsáki, G. (2006). *Rhythms of the Brain*. Oxford university press.

Buzsáki, G., Anastassiou, C. A., and Koch, C. (2012). The origin of extracellular fields and currents — EEG, ECoG, LFP and spikes. *Nature Reviews Neuroscience 2012 13:6*, 13(6):407–420.

Buzsáki, G. and Draguhn, A. (2004). Neuronal oscillations in cortical networks. *Science (New York, N.Y.)*, 304(5679):1926–1929.

Buzsáki, G., Lai-Wo S., L., and Vanderwolf, C. H. (1983). Cellular bases of hippocampal EEG in the behaving rat. *Brain research*, 287(2):139–171.

Canolty, R. T., Edwards, E., Dalal, S. S., Soltani, M., Nagarajan, S. S., Kirsch, H. E., Berger, M. S., Barbare, N. M., and Knight, R. T. (2006). High gamma power is phase-locked to theta oscillations in human neocortex. *Science (New York, N.Y.)*, 313(5793):1626–1628.

Canolty, R. T. and Knight, R. T. (2010). The functional role of cross-frequency coupling. *Trends in Cognitive Sciences*, 14(11):506.

Cogno, S. G., Obenhaus, H. A., Jacobsen, R. I., Donato, F., Moser, M.-B., and Moser, E. I. (2022). Minute-scale oscillatory sequences in medial entorhinal cortex. *bioRxiv*, page 2022.05.02.490273.

Cole, S. and Voytek, B. (2019). Cycle-by-cycle analysis of neural oscillations. *Journal of Neurophysiology*, 122(2):849–861.

Cole, S. R. and Voytek, B. (2017). Brain Oscillations and the Importance of Waveform Shape. *Trends in Cognitive Sciences*, 21(2):137–149.

Cowley, B. R., Snyder, A. C., Acar, K., Williamson, R. C., Yu, B. M., and Smith, M. A. (2020). Slow Drift of Neural Activity as a Signature of Impulsivity in Macaque Visual and Prefrontal Cortex. *Neuron*, 108(3):551–567.

Deng, J., Dong, W., Socher, R., Li, L.-J., Kai Li, and Li Fei-Fei (2010). ImageNet: A large-scale hierarchical image database. pages 248–255.

Donoghue, T., Haller, M., Peterson, E. J., Varma, P., Sebastian, P., Gao, R., Noto, T., Lara, A. H., Wallis, J. D., Knight, R. T., Shestyuk, A., and Voytek, B. (2020). Parameterizing neural power spectra into periodic and aperiodic components. *Nature Neuroscience 2020 23:12*, 23(12):1655–1665.

Engel, A. K., König, P., Kreiter, A. K., and Singer, W. (1991). Interhemispheric synchronization of oscillatory neuronal responses in cat visual cortex. *Science (New York, N.Y.)*, 252(5009):1177–1179.

Fries, P. (2015). Rhythms For Cognition: Communication Through Coherence. *Neuron*, 88(1):220.

Fries, P., Reynolds, J. H., Rorie, A. E., and Desimone, R. (2001). Modulation of oscillatory neuronal synchronization by selective visual attention. *Science (New York, N.Y.)*, 291(5508):1560–1563.

Glaser, J. I., Benjamin, A. S., Chowdhury, R. H., Perich, M. G., Miller, L. E., and Kording, K. P. (2020). Machine Learning for Neural Decoding. *eNeuro*, 7(4):1–16.

Goris, R. L. T., Movshon, J. A., and Simoncelli, E. P. (2014). Partitioning neuronal variability. *Nature Publishing Group*, 17(6).

Gray, C. M., König, P., Engel, A. K., and Singer, W. (1989). Oscillatory responses in cat visual cortex exhibit inter-columnar synchronization which reflects global stimulus properties. *Nature 1989 338:6213*, 338(6213):334–337.

Haider, B., Schulz, D. P., Häusser, M., and Carandini, M. (2016). Millisecond Coupling of Local Field Potentials to Synaptic Currents in the Awake Visual Cortex. *Neuron*, 90(1):35.

Harris, K. D. and Thiele, A. (2011). Cortical state and attention. *Nature reviews. Neuroscience*, 12(9):509–523.

Higley, M. J. and Cardin, J. A. (2022). Spatiotemporal dynamics in large-scale cortical networks. *Current Opinion in Neurobiology*, 77:102627.

Hochreiter, S. and Schmidhuber, J. (1997). Long Short-Term Memory. *Neural Computation*, 9(8):1735–1780.

Hoseini, M. S., Higashikubo, B., Cho, F. S., Chang, A. H., Clemente-Perez, A., Lew, I., Ciesielska, A., Stryker, M. P., and Paz, J. T. (2021). Gamma rhythms and visual information in mouse v1 specifically modulated by somatostatin+ neurons in reticular thalamus. *eLife*, 10.

Klimesch, W. (1999). EEG alpha and theta oscillations reflect cognitive and memory performance: a review and analysis. *Brain research. Brain research reviews*, 29(2-3):169–195.

Klimesch, W. (2013). An algorithm for the EEG frequency architecture of consciousness and brain body coupling. *Frontiers in human neuroscience*, 7.

Lakatos, P., Karmos, G., Mehta, A. D., Ulbert, I., and Schroeder, C. E. (2008). Entrainment of neuronal oscillations as a mechanism of attentional selection. *Science (New York, N.Y.)*, 320(5872):110–113.

Leopold, D. A., Murayama, Y., and Logothetis, N. K. (2003). Very Slow Activity Fluctuations in Monkey Visual Cortex: Implications for Functional Brain Imaging. *Cerebral Cortex*, 13(4):422–433.

Lohani, S., Moberly, A. H., Benisty, H., Landa, B., Jing, M., Li, Y., Higley, M. J., and Cardin, J. A. (2022). Spatiotemporally heterogeneous coordination of cholinergic and neocortical activity. *Nature Neuroscience 2022 25:12*, 25(12):1706–1713.

Luczak, A., Bartho, P., and Harris, K. D. (2013). Gating of sensory input by spontaneous cortical activity. *J Neurosci*, 33(4):1684–1695.

Luczak, A., McNaughton, B. L., and Harris, K. D. (2015). Packet-based communication in the cortex. *Nature reviews. Neuroscience*, 16(12):745–755.

Michalareas, G., Vezoli, J., van Pelt, S., Schoffelen, J. M., Kennedy, H., and Fries, P. (2016). Alpha-Beta and Gamma Rhythms Subserve Feedback and Feedforward Influences among Human Visual Cortical Areas. *Neuron*, 89(2):384–397.

Miller, E. K., Lundqvist, M., and Bastos, A. M. (2018). Working Memory 2.0. *Neuron*, 100(2):463–475.

Nunez-Elizalde, A. O., Krumin, M., Reddy, C. B., Montaldo, G., Urban, A., Harris, K. D., and Carandini, M. (2022). Neural correlates of blood flow measured by ultrasound. *Neuron*, 110(10):1631–1640.

Odean, N. N., Sanayei, M., and Shadlen, M. N. (2023). Transient oscillations of neural firing rate associated with routing of evidence in a perceptual decision. *The Journal of neuroscience : the official journal of the Society for Neuroscience*, pages 2200–22.

Okun, M., Steinmetz, N. A., Lak, A., Dervinis, M., and Harris, K. D. (2019). Distinct Structure of Cortical Population Activity on Fast and Infraslow Timescales. *Cerebral cortex (New York, N.Y. : 1991)*, 29(5):2196–2210.

Pachitariu, M., Steinmetz, N. A., Kadir, S. N., Carandini, M., and Harris, K. D. (2016). Fast and accurate spike sorting of high-channel count probes with KiloSort. *Advances in Neural Information Processing Systems*, 29.

Pandarinath, C., O'Shea, D. J., Collins, J., Jozefowicz, R., Stavisky, S. D., Kao, J. C., Trautmann, E. M., Kaufman, M. T., Ryu, S. I., Hochberg, L. R., Henderson, J. M., Shenoy, K. V., Abbott, L. F., and Sussillo, D. (2018). Inferring single-trial neural population dynamics using sequential auto-encoders. *Nature Methods*, 15(10).

Pedregosa, F., Michel, V., Grisel, O., Blondel, M., Prettenhofer, P., Weiss, R., Vanderplas, J., Cournapeau, D., Pedregosa, F., Varoquaux, G., Gramfort, A., Thirion, B., Grisel, O., Dubourg, V., Passos, A., Brucher, M., Perrot andÉdouardand, M., Duchesnay, a., and Duchesnay, F. (2011). Scikit-learn: Machine Learning in Python Gaël Varoquaux Bertrand Thirion Vincent Dubourg Alexandre Passos PEDREGOSA, VAROQUAUX, GRAMFORT ET AL. Matthieu Perrot. *Journal of Machine Learning Research*, 12:2825–2830.

Penttonen, M. and Buzsáki, G. (2003). Natural logarithmic relationship between brain oscillators. *Thalamus & Related Systems*, 2(2):145–152.

Perrenoud, Q., Fonseca, A. H. d. O., Airhart, A., Bonanno, J., Mao, R., and Cardin, J. A. (2022). Flexible perceptual encoding by discrete gamma events. *bioRxiv*, page 2022.05.13.491832.

Perrenoud, Q., Pennartz, C. M., and Gentet, L. J. (2016). Membrane Potential Dynamics of Spontaneous and Visually Evoked Gamma Activity in V1 of Awake Mice. *PLoS Biology*, 14(2).

Pesaran, B., Pezaris, J. S., Sahani, M., Mitra, P. P., and Andersen, R. A. (2002). Temporal structure in neuronal activity during working memory in macaque parietal cortex. *Nature neuroscience*, 5(8):805–811.

Pletzer, B., Kerschbaum, H., and Klimesch, W. (2010). When frequencies never synchronize: The golden mean and the resting EEG. *Brain Research*, 1335:91–102.

Roopun, A. K., Kramer, M. A., Carracedo, L. M., Kaiser, M., Davies, C. H., Traub, R. D., Kopell, N. J., and Whittington, M. A. (2008). Temporal Interactions between Cortical Rhythms. *Frontiers in neuroscience*, 2(2):145–154.

Sabri, E. (2023). Extra Figures for isoCycle Paper. *Figshare*.

Sabri, E. and Batista-Brito, R. (2023). VIP-Interneurons Control the Effect of Behavioral State on Sensory Responses in Mice Primary Visual Cortex. *Cognitive Computational Neuroscience*, 7:1088–1090.

Sabri, M. M. and Arabzadeh, E. (2018). Information processing across behavioral states: Modes of operation and population dynamics in rodent sensory cortex. *Neuroscience*, 368:214–228.

Saleem, A. B., Lien, A. D., Krumin, M., Haider, B., Rosón, M. R., Ayaz, A., Reinhold, K., Busse, L., Carandini, M., Harris, K. D., and Carandini, M. (2017). Subcortical Source and Modulation of the Narrowband Gamma Oscillation in Mouse Visual Cortex. *Neuron*, 93(2):315–322.

Schneider, M., Broggini, A. C., Dann, B., Tzanou, A., Uran, C., Sheshadri, S., Scherberger, H., and Vinck, M. (2021). A mechanism for inter-areal coherence through communication based on connectivity and oscillatory power. *Neuron*, 109(24):4050.

Schoffelen, J. M., Oostenveld, R., and Fries, P. (2005). Neuronal coherence as a mechanism of effective corticospinal interaction. *Science (New York, N.Y.)*, 308(5718):111–113.

Senzai, Y., Fernandez-Ruiz, A., and Buzsáki, G. (2019). Layer-Specific Physiological Features and Interlaminar Interactions in the Primary Visual Cortex of the Mouse. *Neuron*, 101(3):500–513.

Shadlen, M. N. and Movshon, J. A. (1999). Synchrony unbound: a critical evaluation of the temporal binding hypothesis. *Neuron*, 24(1):67–77.

Singer, W. (1999). Neuronal synchrony: a versatile code for the definition of relations? *Neuron*, 24(1):49–65.

Singer, W. (2018). Neuronal oscillations: unavoidable and useful? *European Journal of Neuroscience*, 48(7):2389–2398.

Sirota, A., Montgomery, S., Fujisawa, S., Isomura, Y., Zugaro, M., and Buzsáki, G. (2008). Entrainment of neocortical neurons and gamma oscillations by the hippocampal theta rhythm. *Neuron*, 60(4):683–697.

Steinmetz, N., Pachitariu, M., Stringer, C., Carandini, M., and Harris, K. (2019). Eight-probe Neuropixels recordings during spontaneous behaviors. *Figshare*.

Syeda, A., Zhong, L., Tung, R., Long, W., Pachitariu, M., and Stringer, C. (2022). Facemap: a framework for modeling neural activity based on orofacial tracking. *bioRxiv*, page 2022.11.03.515121.

Vanhatalo, S., Palva, J. M., Holmes, M. D., Miller, J. W., Voipio, J., and Kaila, K. (2004). Infraslow oscillations modulate excitability and interictal epileptic activity in the human cortex during sleep. *Proceedings of the National Academy of Sciences of the United States of America*, 101(14):5053.

Voytek, B., Canolty, R. T., Shestyuk, A., Crone, N. E., Parvizi, J., and Knight, R. T. (2010). Shifts in gamma phase-amplitude coupling frequency from theta to alpha over posterior cortex during visual tasks. *Frontiers in Human Neuroscience*, 4:191.

Voytek, B., Kramer, M. A., Case, J., Lepage, K. Q., Tempesta, Z. R., Knight, R. T., and Gazzaley, A. (2015). Age-Related Changes in 1/f Neural Electrophysiological Noise. *Journal of Neuroscience*, 35(38):13257–13265.

Wang, X. J. (2010). Neurophysiological and computational principles of cortical rhythms in cognition. *Physiological reviews*, 90(3):1195–1268.

Williams, A. H., Poole, B., Maheswaranathan, N., Dhawale, A. K., Fisher, T., Wilson, C. D., Brann, D. H., Trautmann, E. M., Ryu, S., Shusterman, R., Rinberg, D., Ölveczky, B. P., Shenoy, K. V., and Ganguli, S. (2020). Discovering Precise Temporal Patterns in Large-Scale Neural Recordings through Robust and Interpretable Time Warping. *Neuron*, 105(2).

5 Supplementary Figures

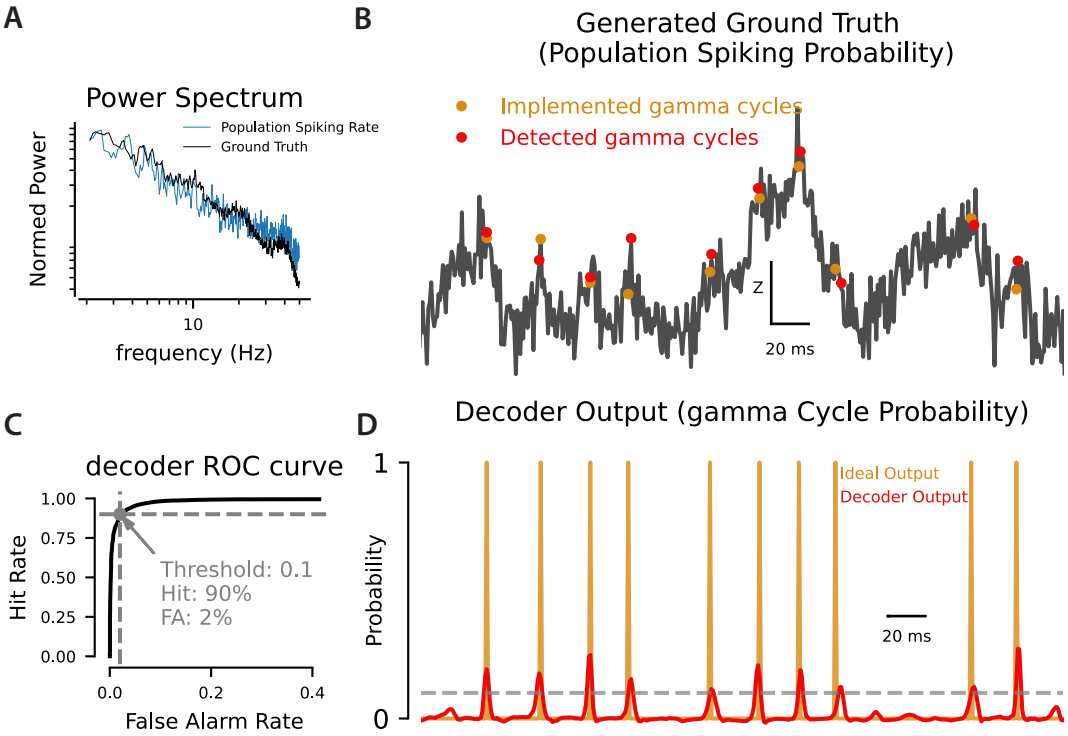

Figure S1. Decoder Characteristics. A. The blue trace represents the average power spectrum of the population spiking rate from 29 recording sites (4 S1 recording sites, 5 V1 recording sites, and 22 recording sites across the brain in Mouse 1 from Steinmetz et al. (2019)). The black trace is the power spectrum of the generated ground-truth. The ground truth was generated using six cycle types (high gamma, gamma, beta, alpha, theta, and delta see Figure 1A). Each cycle type occurred with a 60% chance. The width of each cycle at each instance was randomly jittered by adding a value derived from a normal distribution with $\mu = 0$ and σ equal to 30% of the cycle width (e.g. 6.6 ms for the gamma cycle). After normalizing the signal to range between 0 and 1, the noise was introduced by adding a random value, derived from a normal distribution with $\mu = 0$ and $\sigma = 0.05$, at each time point. **B.** An example period of the ground truth spiking probability. The decoder was run to detect the gamma cycles on this signal. The orange dots show the center of each implemented gamma cycle in the signal, and the red dots are the detected gamma cycles after thresholding and peak detection on the output of the decoder (see the next panels). **C.** The decoder's ROC curve with the threshold used for the cycle detection. **D.** The decoder output (red trace) in response to the signal in B is compared to the ideal output (orange trace), which is zero everywhere except at the center of the gamma cycles. The dashed line is the threshold level (panel C) chosen to decide the cycle time based on the decoder output.

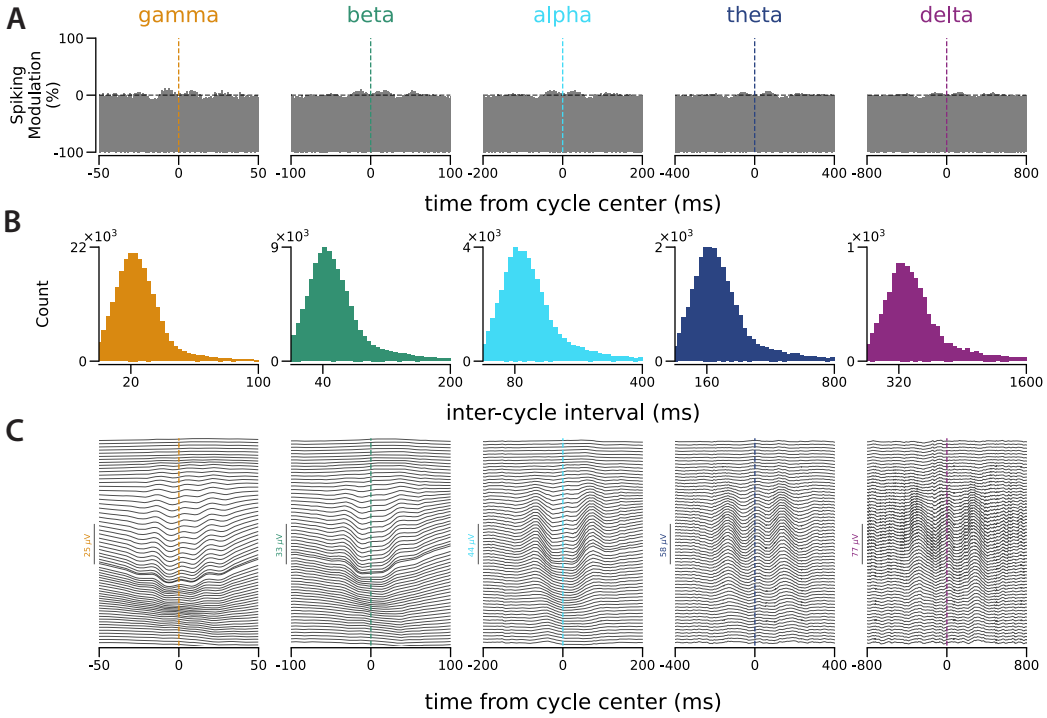

Figure S2. Spiking Modulations Disappear with Shifted Cycle Times. Same analyses as in panels D-F of Figure 1, when a random jitter of up to half a cycle width is added to or subtracted from each detected cycle time.

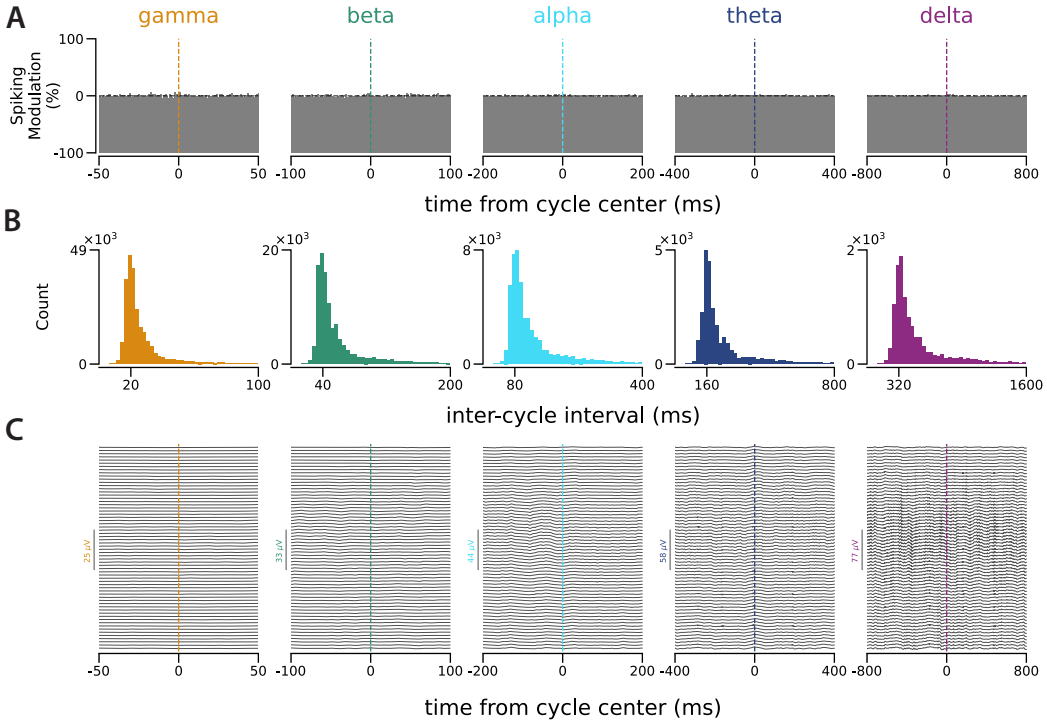

Figure S3. Spiking Modulations Disappear with Shuffled Cycle Times. Same analyses as in panels **D-F** of Figure 1, when the detected cycle times were shuffled while the distribution of the inter-cycle intervals has been kept the same as for the original cycle times.

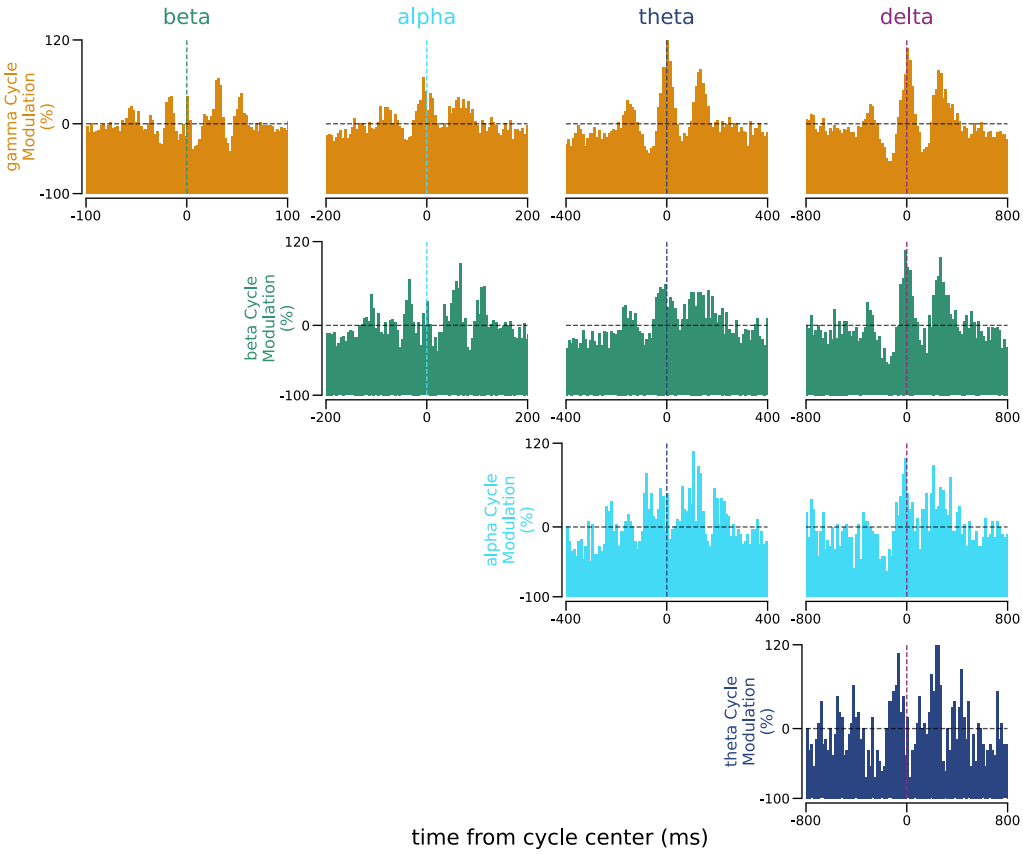

Figure S4. Relations between all Pairs of Cycles. A. Similar to Figure 1G, between all pairs of cycles (p=0.5 used as the threshold level for cycle detection in this figure to reduce the chance of false alarms).

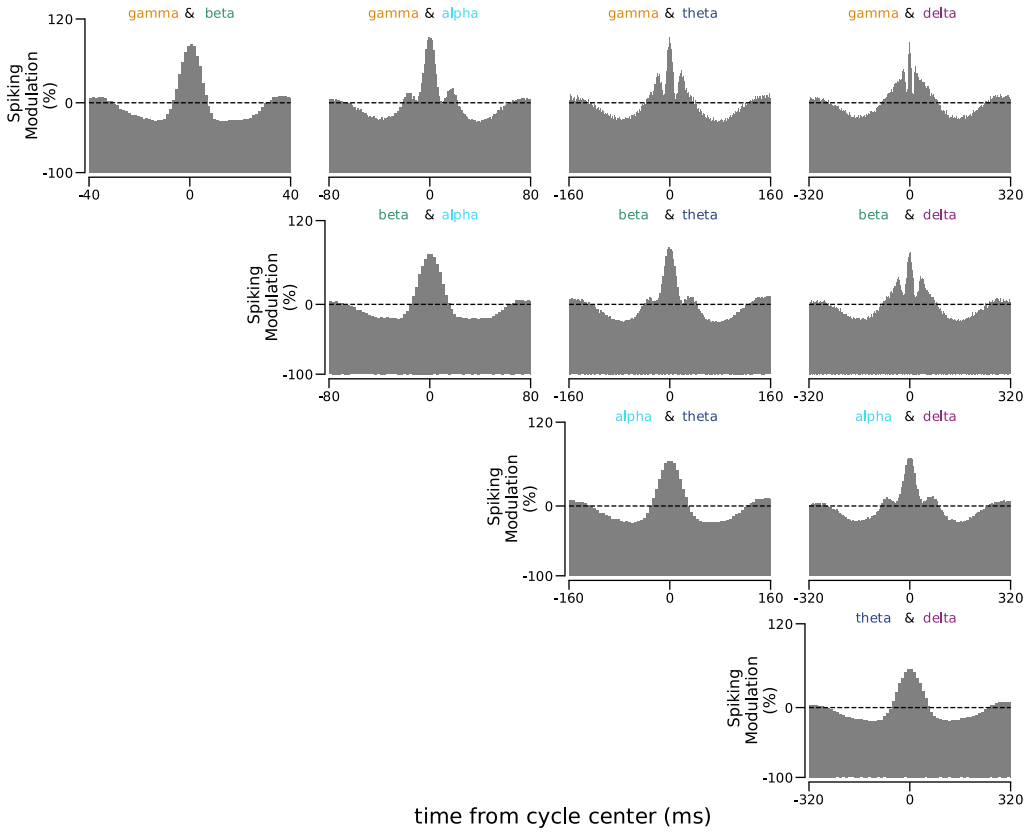

Figure S5. Distributions of Spiking Around the Times of Co-occurrence of the Cycle Pairs as in Figure S4. Similar to Figure 1H, with times of co-occurrence for all pairs of cycles (p=0.1 used as the threshold level for cycle detection in this figure).

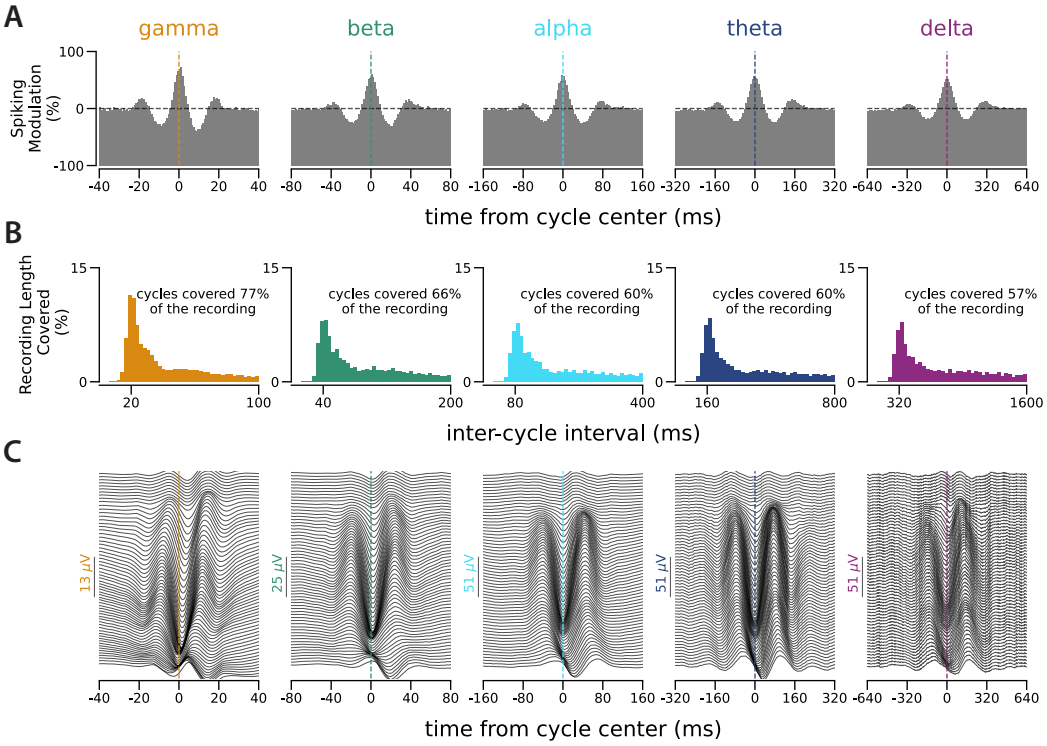

Figure S6. Cycle Detection in Primary Somatosensory Cortex (S1). Similar to Figure 1D-E, for cycles detected from 49 neurons recorded simultaneously in mouse S1 for 8370 seconds.

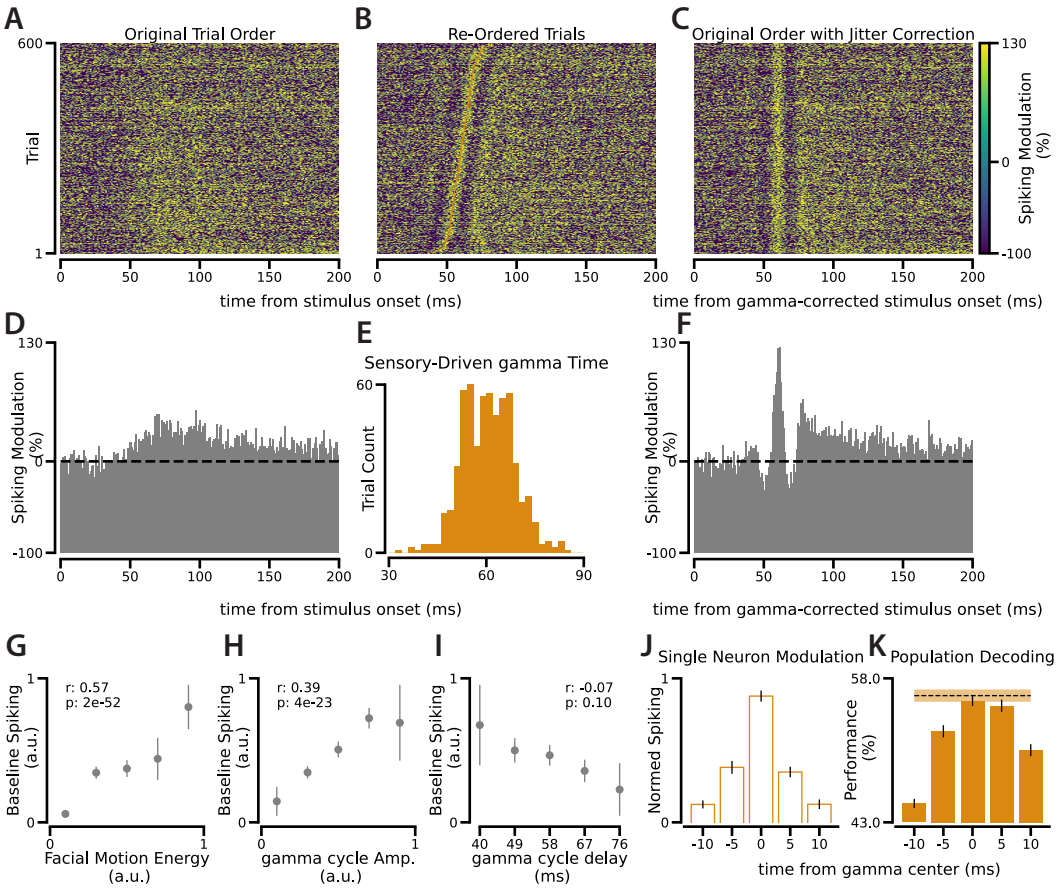

Figure S7. Extra Experiment for Figure 2. Similar analyses as in Figure 2 for a recording in another animal. In this recording session, 58 neurons were simultaneously recorded while drifting gratings were shown to the animal.

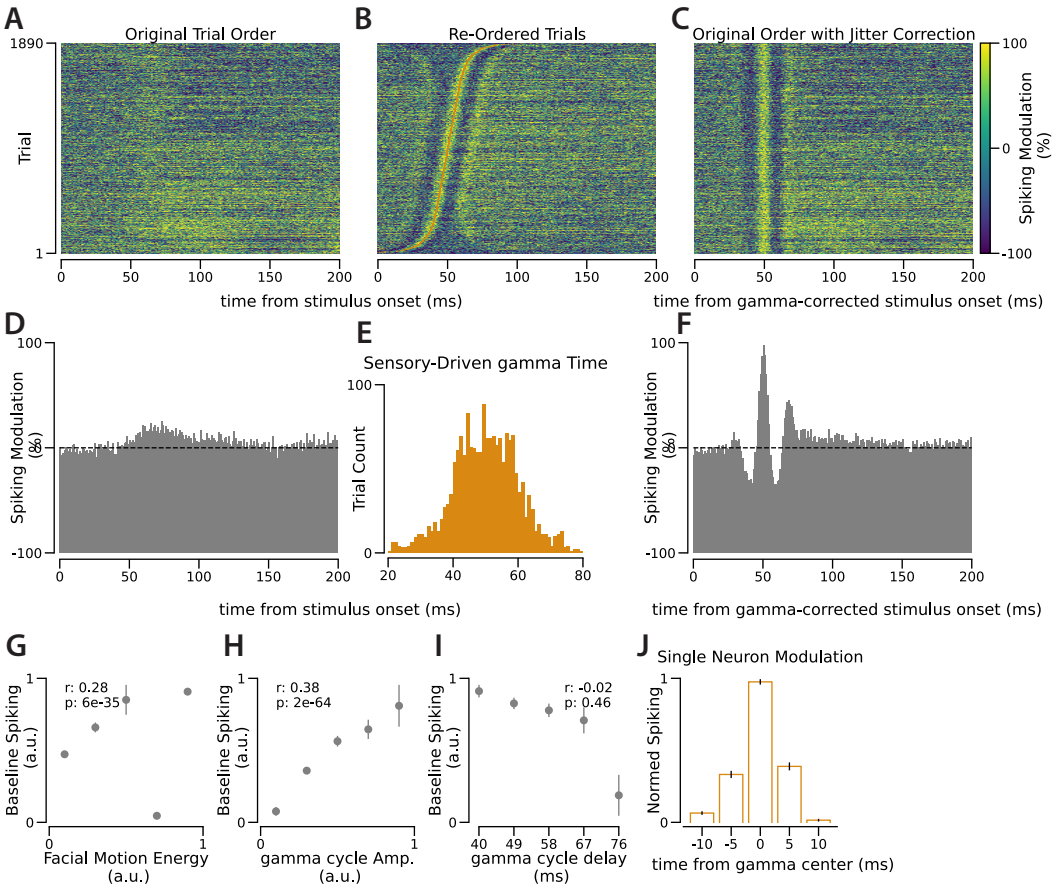

Figure S8. Extra Experiment for Figure 2. Similar analyses as in Figure 2 for a recording in another animal. In this recording session, 56 neurons have been simultaneously recorded, while 70 distinct natural stimuli during 1890 trials have been shown to the animal.

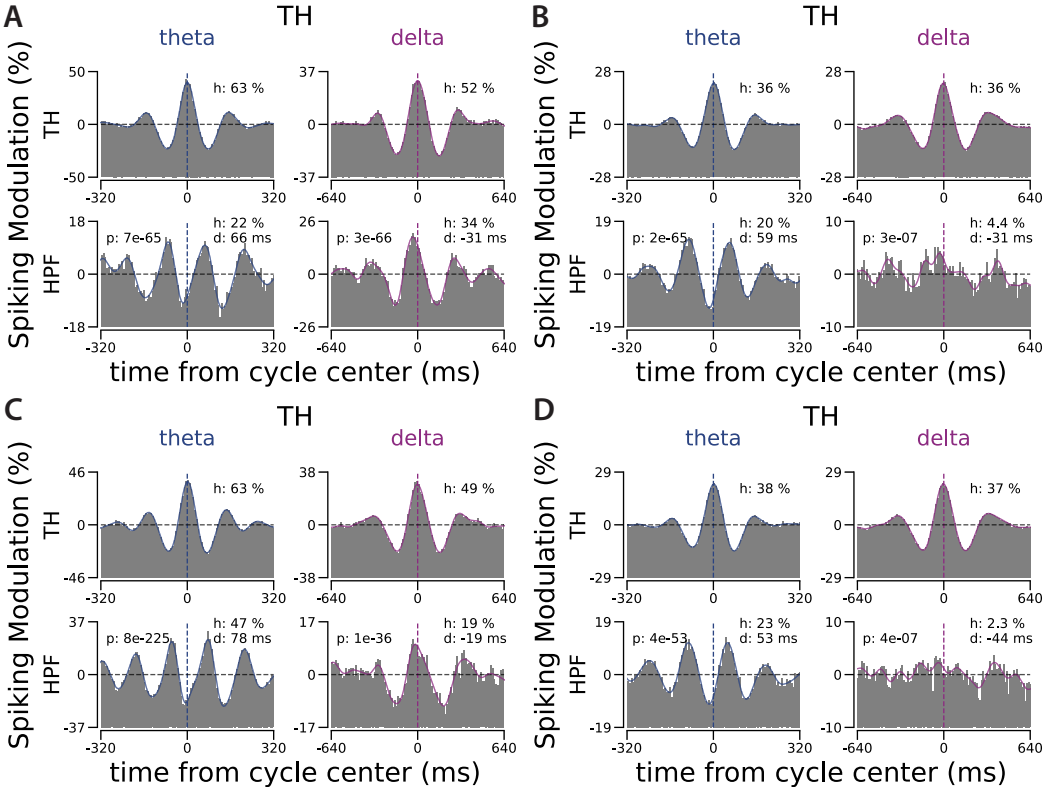

Figure S9. Half Session Controls for Figure 3A-B. Similar to Figure 3A-B when the cycles detected in each session's first and second half have been used separately to compute the spiking distribution. **A-B.** First half. **C-D.** Second half.

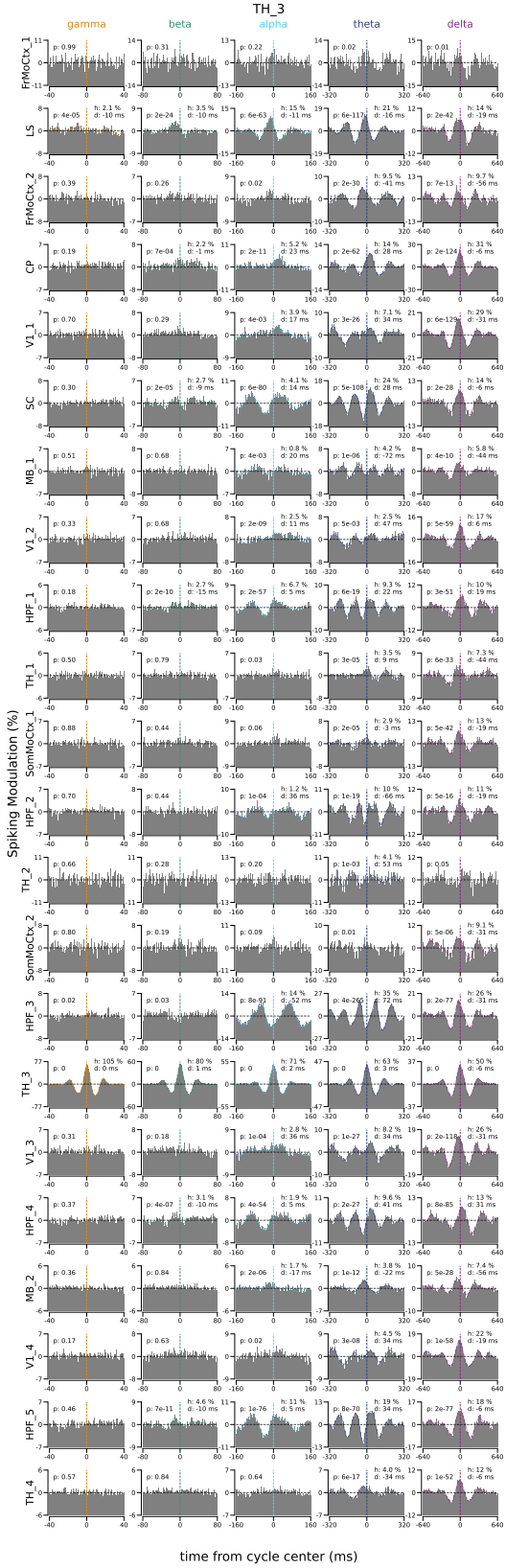

Figure S10. All Regions Relative to The Cycles in Thalamus. Similar to Figure 3A for all the recorded regions relative to the cycles detected in Thalamaus (site TH_3 in mouse 1, named Kerbs, in the dataset from Steinmetz et al. (2019)). If there is more than one recording site in one brain region, the recording sites are differentiated with a number added to the end of the region name (e.g., TH_1, TH_2, etc.). Similar figures for all regions in this animal can be found at Sabri (2023).

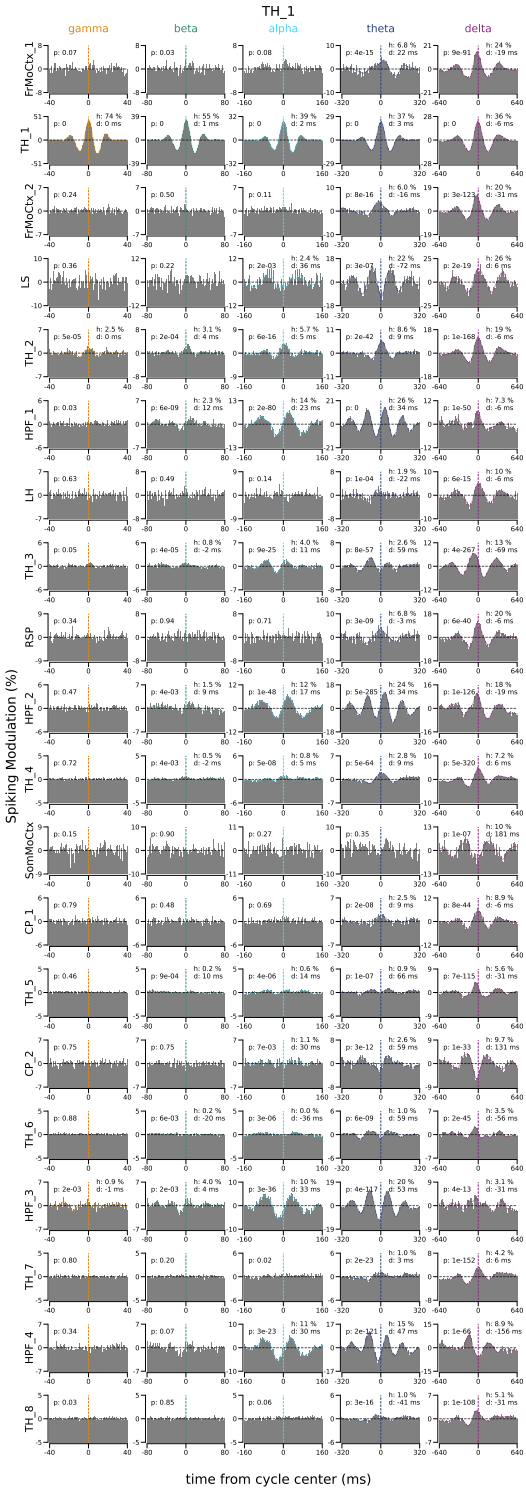

Figure S11. All Regions Relative to The Cycles in Thalamus. Similar to Figure 3B for all the recorded regions relative to the cycles detected in Thalamus (site TH_1 in mouse 3, named Robbins, in the dataset from Steinmetz et al. (2019)). If there is more than one recording site in one brain region, the recording sites are differentiated with a number added to the end of the region name (e.g., TH_1, TH_2, etc.). Similar figures for all regions in 3 animals can be found at Sabri (2023).

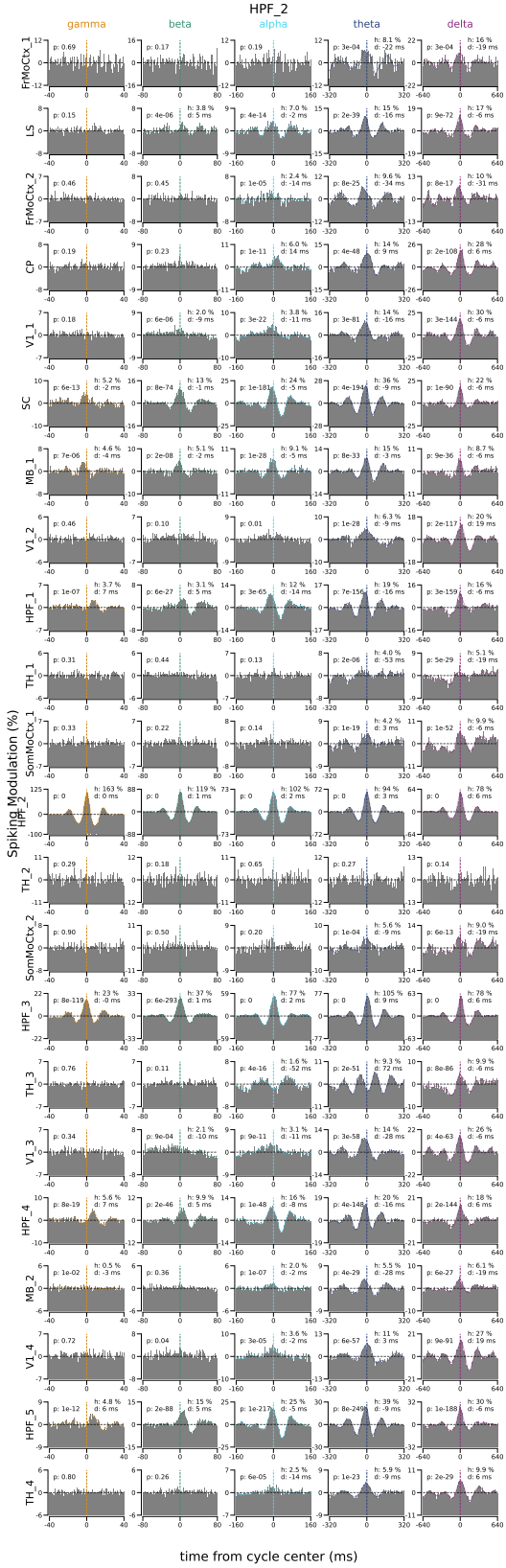

Figure S12. All Regions Relative to The Cycles in Hippocampus. Similar to Figure 3A-B for all the recorded regions relative to the cycles detected in Hippocampus (site HPF_2 in mouse 1, named Kerbs, in the dataset from Steinmetz et al. (2019)). If there is more than one recording site in one brain region, the recording sites are differentiated with a number added to the end of the region name (e.g., TH_1, TH_2, etc.). Similar figures for all regions in 3 animals can be found at Sabri (2023).

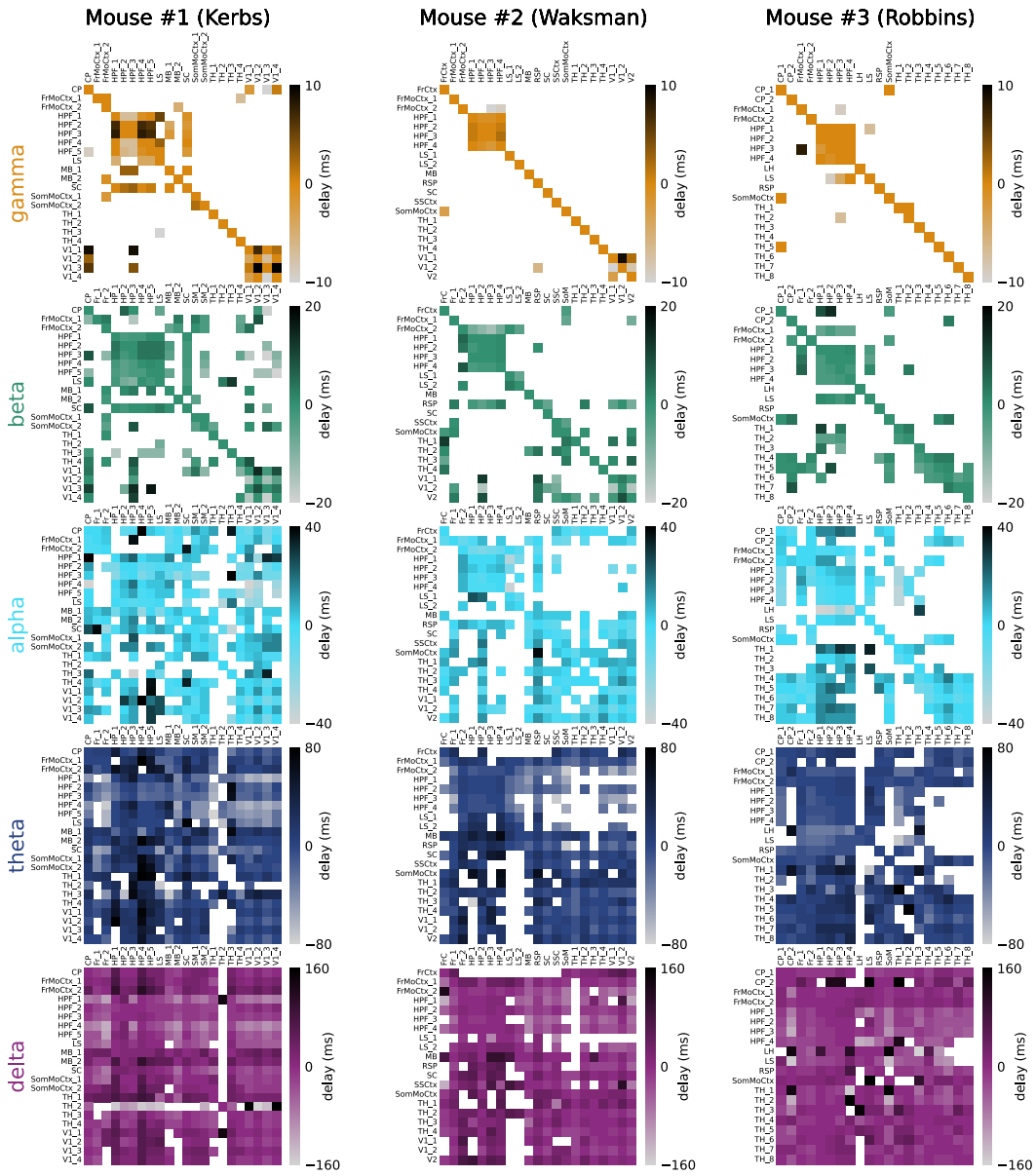

Figure S13. Across Regions Delay from gamma to delta for 3 Animals in Steinmetz et al. (2019). Similar to Figure 3C for gamma, beta, alpha, theta, and delta cycles across all regions in 3 animals. If the pattern of correlated activity between two regions is not significant (see Methods), then the corresponding cell in the delay matrix is left blank. Patterns of correlated activity across regions, from which these delays were derived, can be found at Sabri (2023).

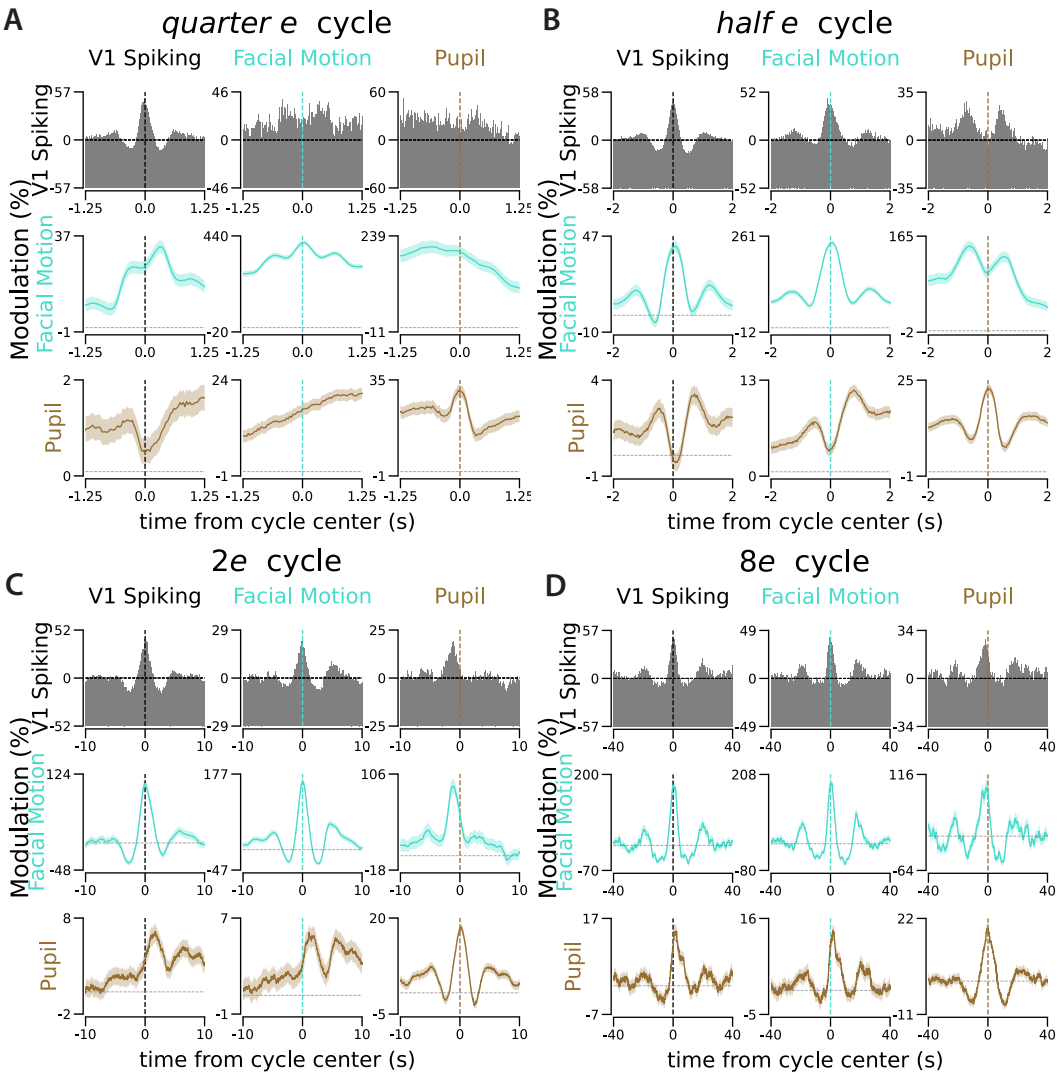

Figure S14. Correlated Activity between Pupil Size, Facial Motion, and V1 Spiking During $quarter\ e$**,** $half\ e$**,** $2e$**, and** $8e$ **Cycles.** Similar to Figure 4B&E for four other slow cycles.

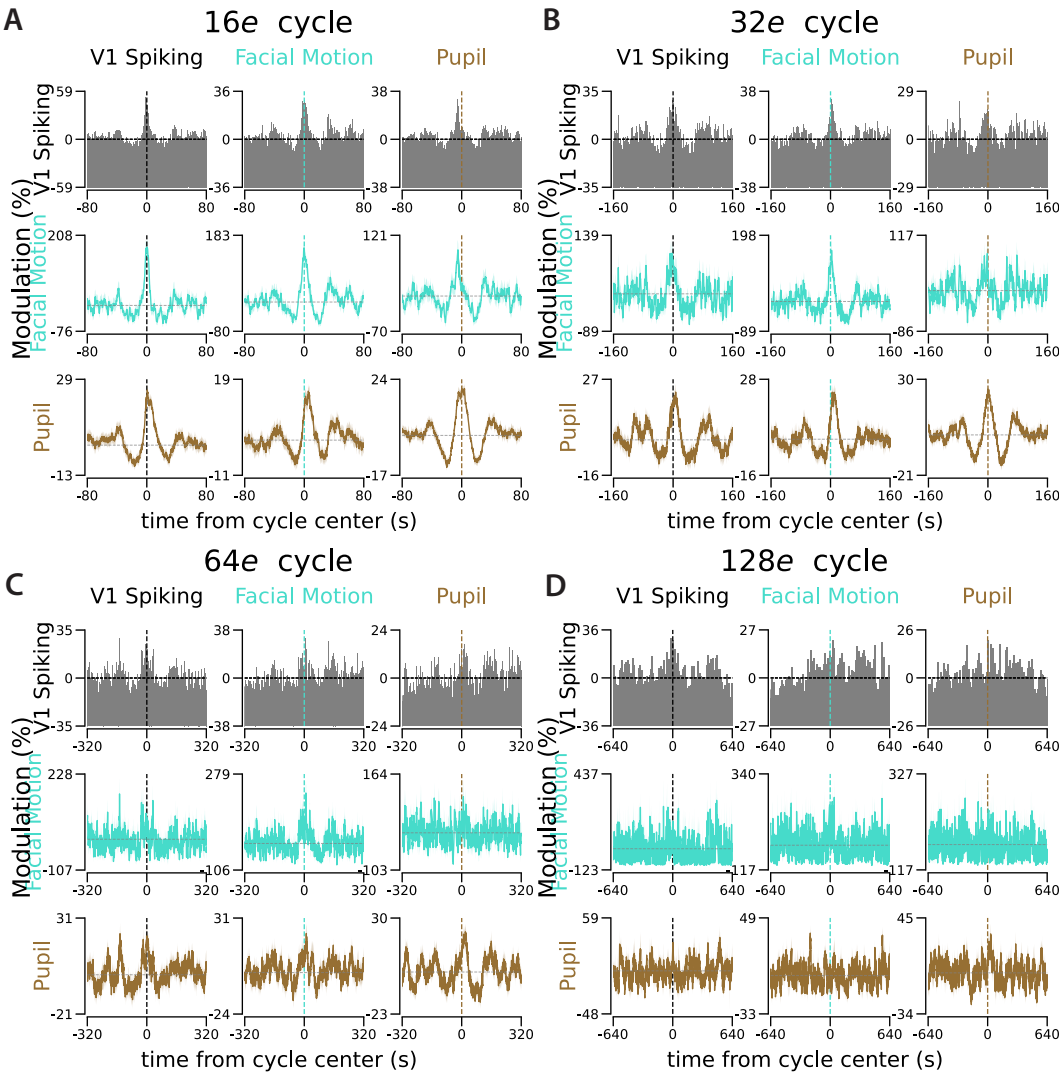

Figure S15. Correlated Activity between Pupil Size, Facial Motion, and V1 Spiking During $16e$**,** $32e$**,** $64e$**, and** $128e$ **Cycles.** Similar to Figure 4B&E for four other slow cycles.

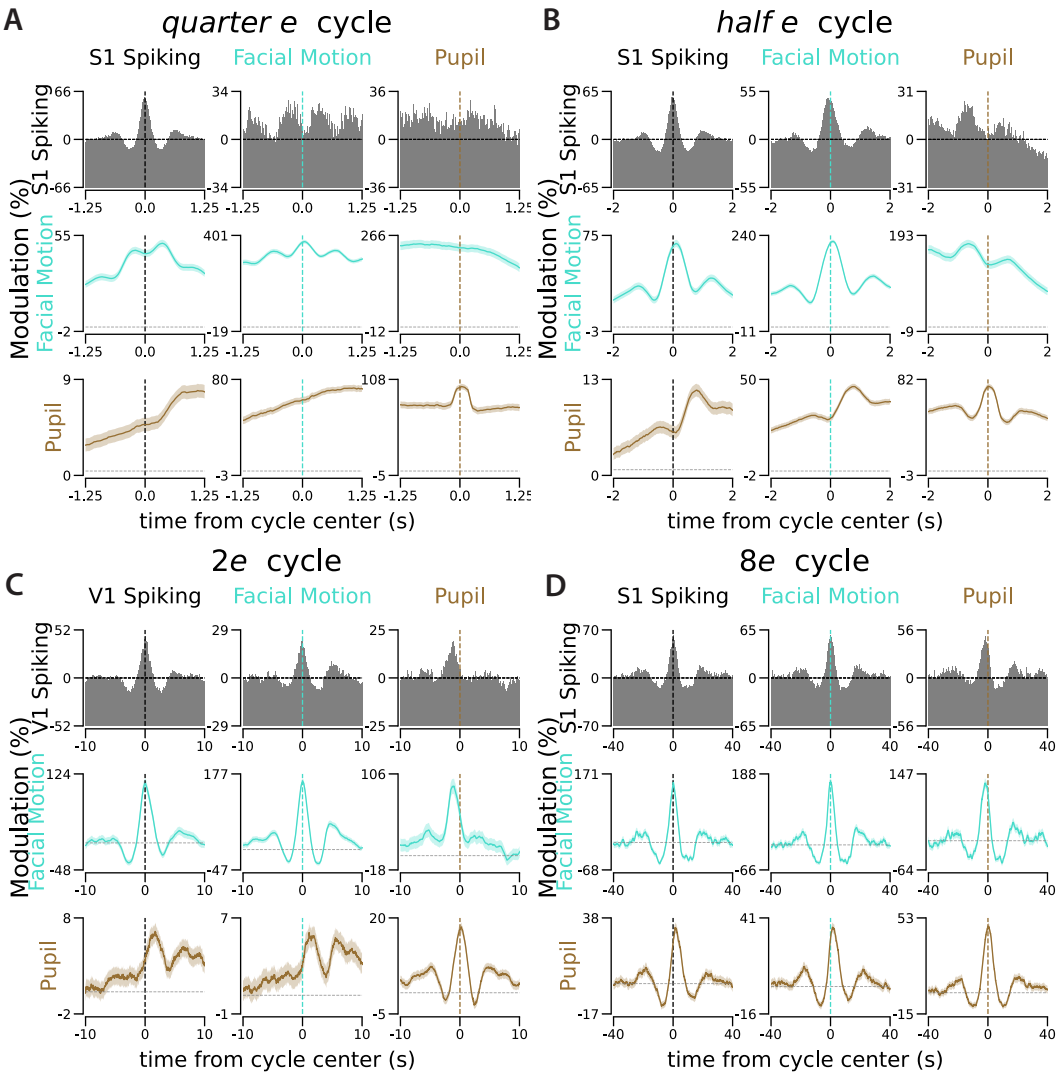

Figure S16. Correlated Activity between Pupil Size, Facial Motion, and S1 Spiking During $quarter\ e$**,** $half\ e$**,** $2e$**, and** $8e$ **Cycles.** Similar to Figure 4C&F for four other slow cycles.

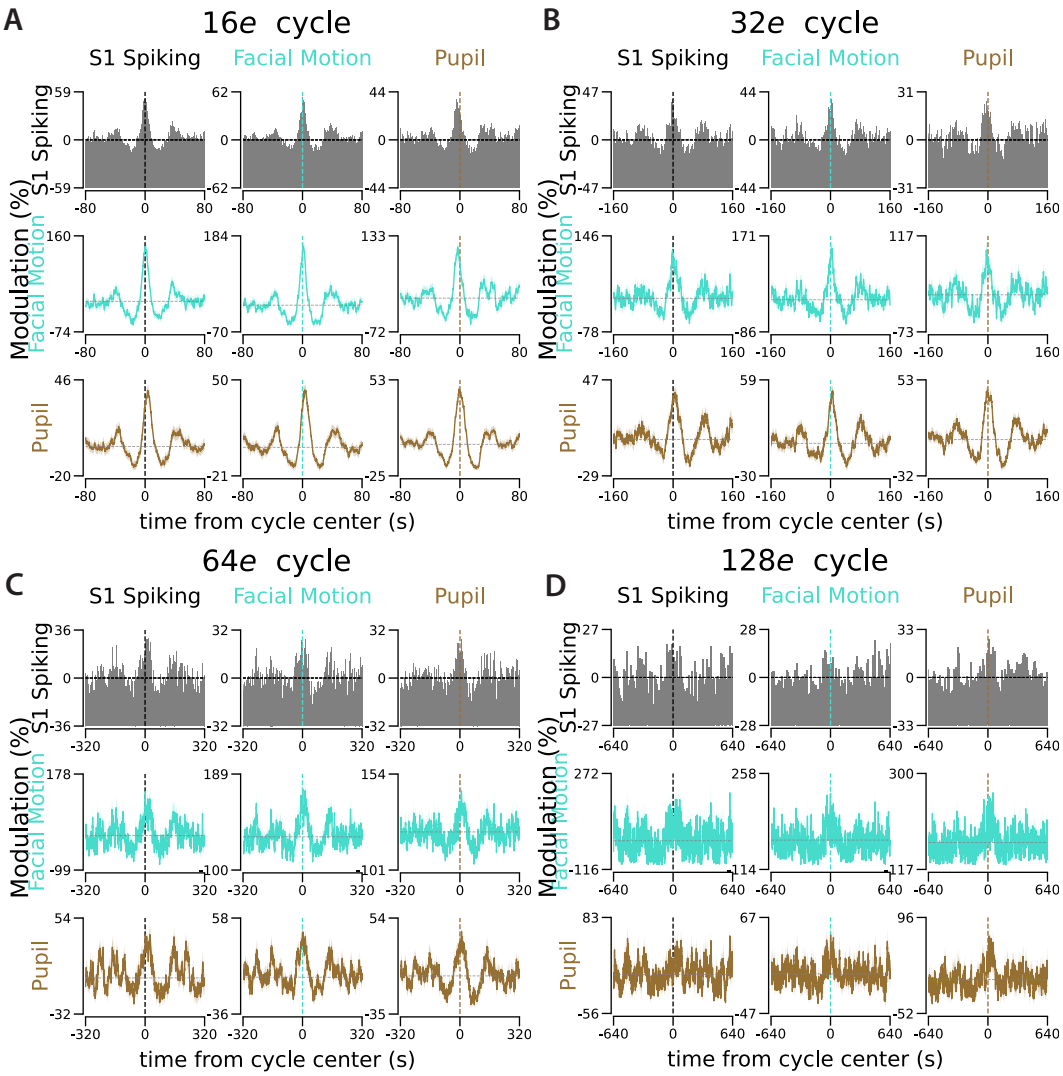

Figure S17. Correlated Activity between Pupil Size, Facial Motion, and S1 Spiking During $16e$**,** $32e$**,** $64e$**, and** $128e$ **Cycles.** Similar to Figure 4C&F for four other slow cycles.

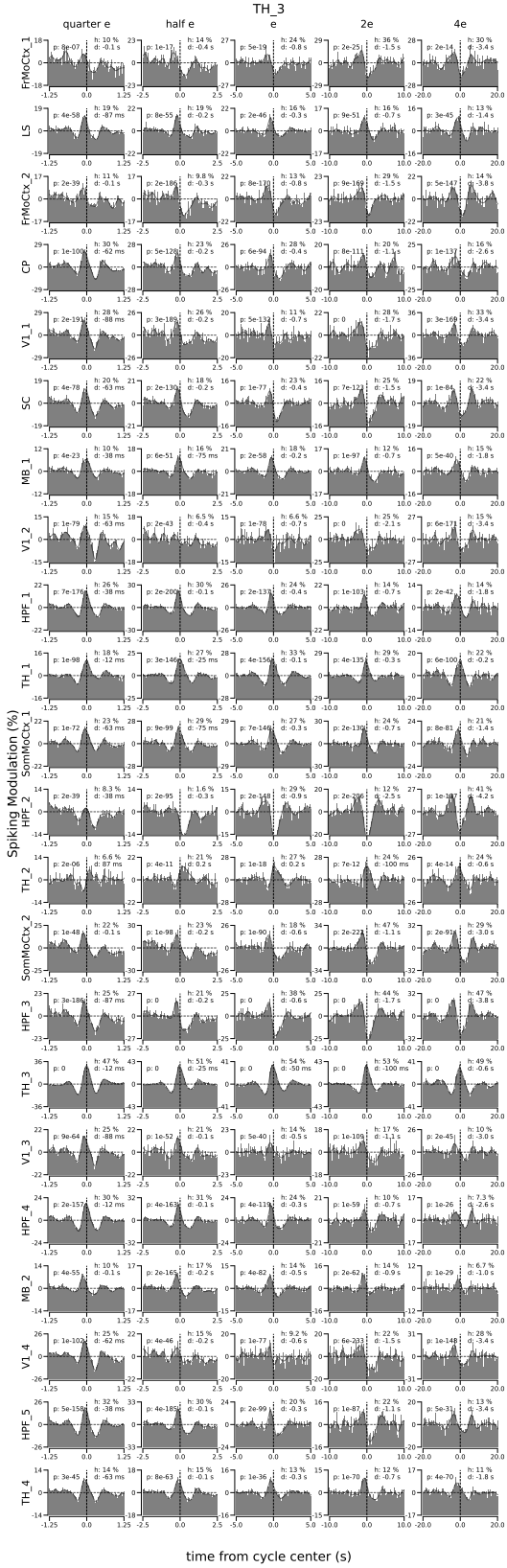

Figure S18. All Regions Relative to The Cycles in Thalamus. Similar to Figure 5A for all the recorded regions relative to the cycles detected in Thalamus (site TH_3 in mouse 1, named Kerbs, in the dataset from Steinmetz et al. (2019)). If there is more than one recording site in one brain region, the recording sites are differentiated with a number added to the end of the region name (e.g., TH_1, TH_2, etc.). Similar figures for all regions in 3 animals can be found at Sabri (2023).

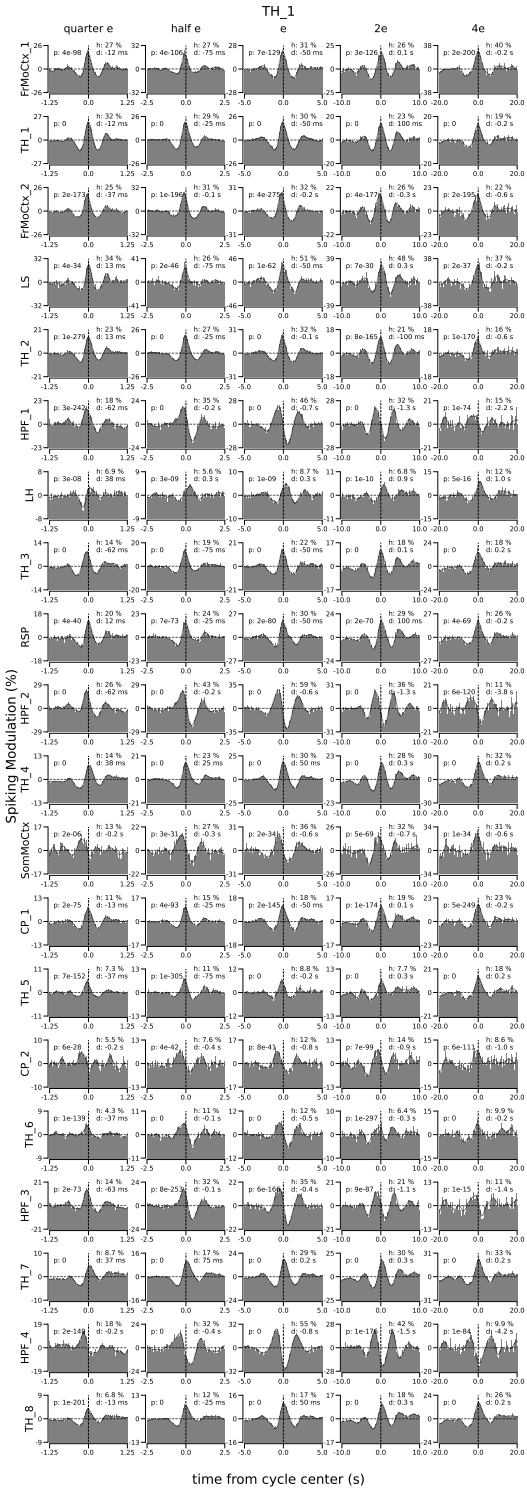

Figure S19. All Regions Relative to The Cycles in Thalamus. Similar to Figure 5B for all the recorded regions relative to the cycles detected in Thalamus (site TH_1 in mouse 3, named Robbins, in the dataset from Steinmetz et al. (2019)). If there is more than one recording site in one brain region, the recording sites are differentiated with a number added to the end of the region name (e.g., TH_1, TH_2, etc.). Similar figures for all regions in 3 animals can be found at Sabri (2023).

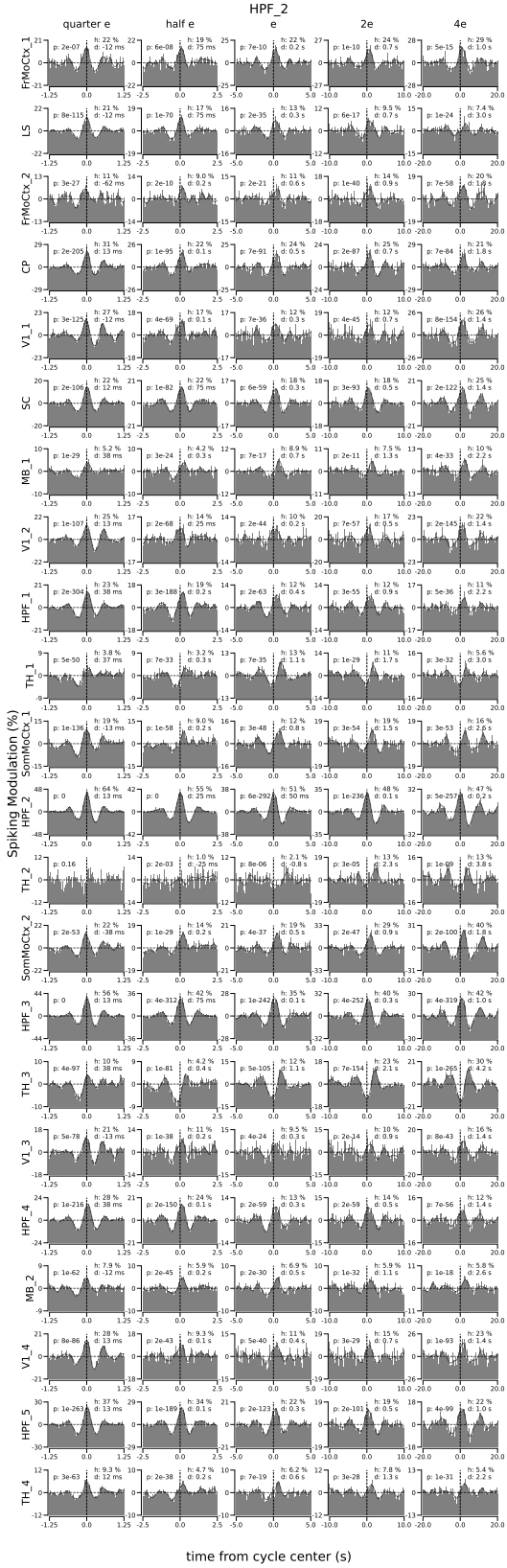

Figure S20. All Regions Relative to The Cycles in Hippocampus. Similar to Figure 5A-B for all the recorded regions relative to the cycles detected in Hippocampus (site HPF_2 in mouse 2, named Waksman, in the dataset from Steinmetz et al. (2019)). If there is more than one recording site in one brain region, the recording sites are differentiated with a number added to the end of the region name (e.g., TH_1, TH_2, etc.). Similar figures for all regions in 3 animals can be found at Sabri (2023).

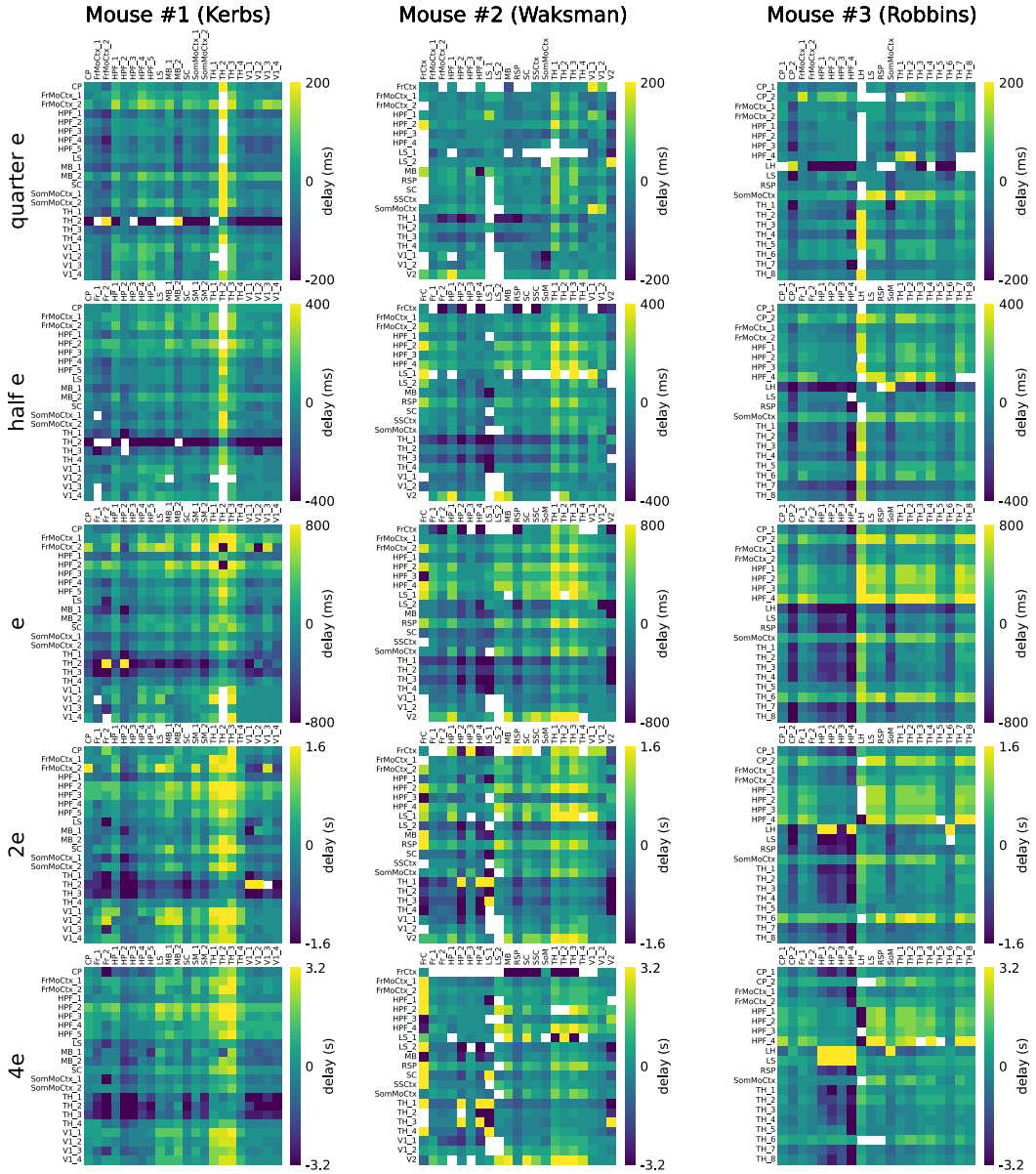

Figure S21. Across Regions Delay from $quartere$ **to** $4e$ **for 3 Animals in Steinmetz et al. (2019).** Similar to Figure 5C for $quartere$, $half e$, e, $2e$, and $4e$ cycles across all regions in 3 animals. If the pattern of correlated activity between two regions is not significant (see Methods), then the corresponding cell in the delay matrix is left blank. Patterns of correlated activity between regions, from which these delays were derived, can be found at Sabri (2023).

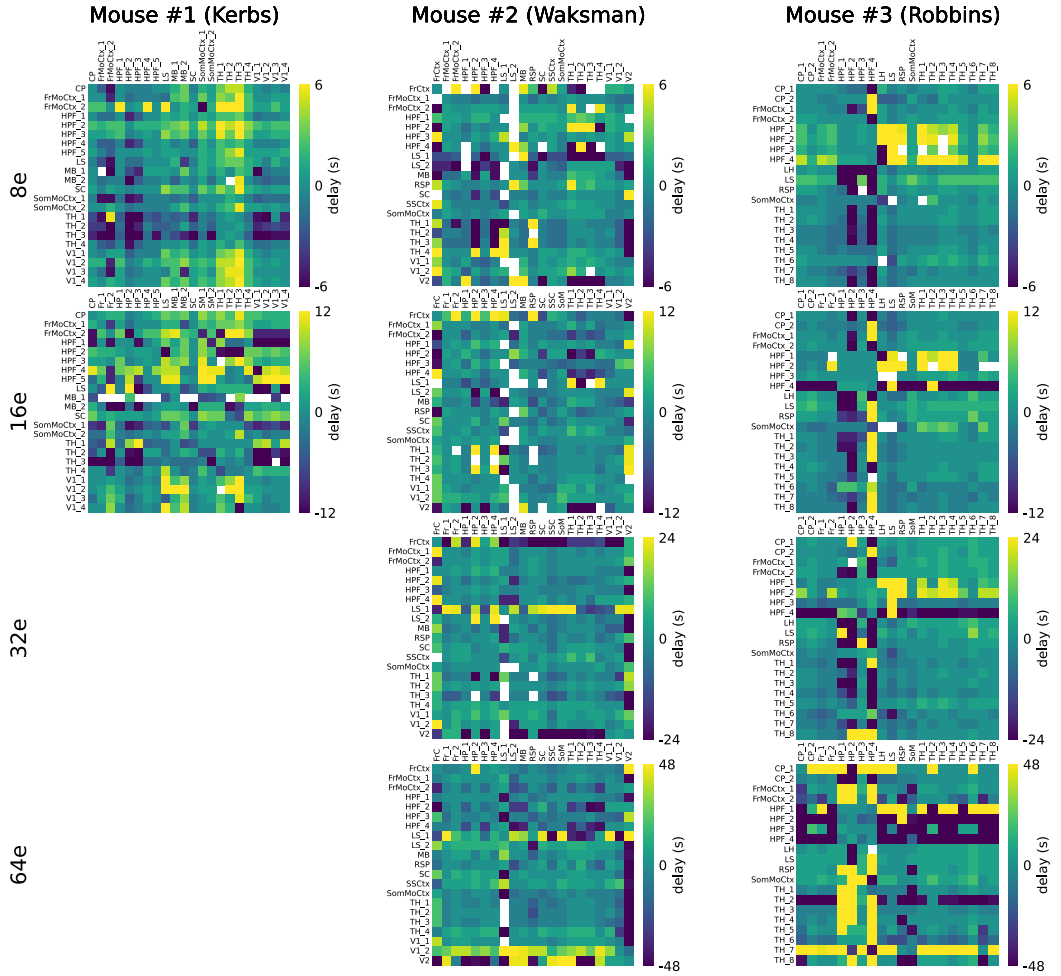

Figure S22. Across Regions Delay from $8e$ **to** $128e$ **for 3 Animals in Steinmetz et al. (2019).** Similar to Figure 5C for $8e$, $16e$, $32e$, and $64e$ cycles across all regions in 3 animals. If the pattern of correlated activity between two regions is not significant (see Methods), then the corresponding cell in the delay matrix is left blank. Patterns of correlated activity between regions, from which these delays were derived, can be found at Sabri (2023).

6 Supplementary Notes

6.1 Cycles and Power Spectrum Schematics in Figure 1.

To generate the panels A and B in Figure 1, we used the function $f(t)$, which is a solution for the motion equation of a harmonic oscillator[1]:

$$y''(x) + y(x) = 0, \qquad x(t) = 2\pi \log_2 \tfrac{t}{e}, \qquad f(t) = y(x(t))$$

$$t^2 f''(t) + t f'(t) + \left(\tfrac{2\pi}{\log 2}\right)^2 f(t) = 0, \qquad \boldsymbol{f(t) = -\cos(2\pi \log_2 \tfrac{t}{e})}$$

[1] https://math.stackexchange.com/questions/139881/how-to-construct-and-oscillation-with-exponentially-gro